

1 **Where does the dust deposited over the Sierra Nevada snow come from?**

2

3 Huilin Huang<sup>1\*</sup>, Yun Qian<sup>1\*</sup>, Ye Liu<sup>1</sup>, Cenlin He<sup>2</sup>, Jianyu Zheng<sup>3,4</sup>, Zhibo Zhang<sup>3,4</sup>, Antonis Gkikas<sup>5</sup>

4

5 <sup>1</sup>Atmospheric Sciences and Global Change Division, Pacific Northwest National Laboratory, Richland, WA,  
6 USA

7 <sup>2</sup>Research Applications Laboratory, National Center for Atmospheric Research, Boulder, CO, USA

8 <sup>3</sup>Department of Physics, University of Maryland Baltimore County, Baltimore, MD, USA

9 <sup>4</sup>Joint Center for Earth Systems Technology, University of Maryland Baltimore County, Baltimore, MD, USA

10 <sup>5</sup>Institute for Astronomy, Astrophysics, Space Applications and Remote Sensing, National Observatory of  
11 Athens, Athens, Greece

12

13 \*Corresponding to: Huilin Huang, [Huilin.huang@pnnl.gov](mailto:Huilin.huang@pnnl.gov); Yun Qian, [Yun.Qian@pnnl.gov](mailto:Yun.Qian@pnnl.gov)

14

15

16

17 Submitted to Atmospheric Chemistry and Physics

18

19 **Abstract**

20 Mineral dust contributes up to one-half of surface aerosol loading in spring over the southwestern U.S.,  
21 posing an environmental challenge that threatens human health and the ecosystem. Using the self-  
22 organizing map (SOM) analysis with dust deposition and fluxes data from WRF-Chem and Modern-Era  
23 Retrospective analysis for Research and Applications, Version 2 (MERRA-2), we identify four typical dust  
24 transport patterns across the Sierra Nevada, associated with the mesoscale winds, Sierra-Barrier-Jets (SBJ),  
25 North-Pacific-High (NPH), and long-range cross-Pacific westerlies, respectively. We find that dust emitted  
26 from the Central Valley is persistently transported eastward, while dust from the Mojave Desert and Great  
27 Basin influences the Sierra Nevada during mesoscale transport occurring mostly in winter and early spring.  
28 Asian dust reaching the mountain range comes either from the west through straight isobars (cross-Pacific  
29 transport) or from the north in the presence of the NPH. Extensive dust depositions are found on the west  
30 slope of the mountain, contributed by Central Valley emissions and cross-Pacific remote transport.  
31 Especially, the SBJ-related transport produces deposition through landfalling atmospheric rivers, whose  
32 frequency might increase in a warming climate.

## 33 **1. Introduction**

34           The emission, transport, and deposition of mineral dust (hereafter dust) are processes  
35 receiving increasing interest from the scientific community (Sarangi et al., 2020). Dust emission is an  
36 integral part of aridification and mirrors the effects of climatic change and anthropogenic land use on global  
37 drylands (Duniway et al., 2019). Airborne dust interacts with Earth’s climate system by altering radiation  
38 budget and cloud lifetime and amount (Forster et al., 2007; Haywood et al., 2005; Huang et al., 2019).  
39 Research has indicated that exposure to dust particles can cause respiratory infections, heart disease, and  
40 chronic obstructive pulmonary disease (COPD) (Laden et al., 2006; Lim et al., 2012; Crooks et al., 2016).  
41 A significant association between dust exposure and increased mortality has been reported, but there is no  
42 consensus in this regard to date (Giannadaki et al., 2014). The deposition of dust on snow surface influences  
43 snow albedo, further contributing to anthropogenic climate change as early as the 1970s (Qian et al., 2009;  
44 Qian et al., 2014; Skiles et al., 2018).

45           Dust over the southwestern U.S., particularly in California and Nevada states, is an important  
46 aerosol type contributing to more than half of surface aerosol concentrations in spring (Kim et al., 2021).  
47 Covered by dry soil with large gaps and sparse vegetation, the surrounding Mojave Desert, Sonoran Desert,  
48 and Great basin are susceptible to wind erosion (Okin et al., 2006; Duniway et al., 2019). The dry or  
49 ephemeral lakes in the deserts produce very fine dust containing toxic inorganic constituents (Goldstein et  
50 al., 2017). In addition, anthropogenic land-use practices – e.g., agriculture and human settlement, have  
51 greatly disturbed crustal biomass and produced windblown dust along the west coast (Pappagianis and  
52 Einstein, 1978; Clausnitzer and Singer, 2000; Neff et al., 2008). Furthermore, cross-Pacific dust transported  
53 from Asia and Africa to the Sierra Nevada range is widely reported (Ault et al., 2011; Creamean et al., 2014;  
54 Creamean et al., 2013). The surface dust concentration has been found to increase in the past two decades  
55 during spring at sites across the Southwest (Tong et al., 2017; Hand et al., 2017; Brahney et al., 2013), and  
56 the onset of dust season is shifting earlier in response to climate change (Hand et al., 2016). The elevated  
57 dust emission and earlier dust season are supposed to lead to a spectrum of environmental and societal

58 impacts in the most populated U.S. state. Especially, the resultant dust deposition on mountain snow  
59 decreases snow albedo and produces a radiation forcing of 0-14.6 W m<sup>-2</sup> during the melting season (Huang  
60 et al., 2022a), shifting snowmelt timing to earlier dates and further increasing California's vulnerability to  
61 water resource fluctuations (Wu et al., 2018; Huang et al., 2022b). With its complex terrains, frequently  
62 varying microclimate, and coexisting sources from both local and remote regions, the Sierra Nevada area  
63 is an interesting region for studying dust transport and its response to climate change.

64 Characterization of dust emission, transport, and deposition across the Sierra Nevada has been  
65 investigated using various data. Isotopic analyses (i.e., concentrations of Pb, Nd) are widely used to  
66 distinguish and quantify the respective contribution of dust emission from local (dried Owen Lakes),  
67 regional (Central Valley and the Mojave Desert), and global sources (Asia and Africa) on the dust  
68 deposition on the mountain (Muhs et al., 2007; Jardine et al., 2021; Aciego et al., 2017; Aarons et al., 2019).  
69 Their source attribution has been generally confirmed by the analyses of dust particle size and composition  
70 (Creamean et al., 2014; Creamean et al., 2013; Reheis and Kihl, 1995). The isotopic and composition  
71 analyses have been commonly used with back-trajectory modeling to further identify the dust transport  
72 pathway from the source to the deposition location (Vicars and Sickman, 2011; Creamean et al., 2014;  
73 Creamean et al., 2013). Yet, these analyses generally retrieve dust sources in a short time and at a specific  
74 location. Alternatively, ground-based measurement networks were established in the 1990s and provide  
75 long-term trends of dust concentrations and the interannual variability across multiple sites (Hand et al.,  
76 2017; Achakulwisut et al., 2017; Hand et al., 2016). However, they do not contain information on dust  
77 origins and atmospheric conditions responsible for dust transport. Satellite retrievals were less commonly  
78 used to study dust characteristics across the Sierra Nevada (Lei and Wang, 2014), mainly due to the poor  
79 data coverage caused by cloud contamination in the region.

80 Global and regional climate-chemistry models have been widely used to understand the drives of  
81 the variability of dust and quantify the role of regional and remote transport, filling the gaps in the  
82 observations (Chin et al., 2002; Chin et al., 2007; Kim et al., 2021; Wu et al., 2017). While dust emissions  
83 and transport have been generally studied, there lacks a connection between dust emissions from the source



84 region and the timing, location, and amount of dust deposition to the Sierra Nevada snow. The isotopic and  
 85 composition analyses attribute dust sources at a few sites. But to our knowledge, no regional  
 86 characterization has been conducted on how dust is transported to the Sierra Nevada after emissions from  
 87 adjacent drylands and remote continents and when, where, and how much depositions occur for dust  
 88 transported through different pathways. The connection between dust emissions, transport pathways, and  
 89 deposition to snow would facilitate the prediction of future changes in dust regimes and the corresponding  
 90 climate impact, enabling more efficient management practices. With a focus on the dust that influences the  
 91 Sierra Nevada, this study investigates 1) Where does the dust come from? 2) How is dust transported to the  
 92 mountain from the sources? 3) How is the dust deposited on the Sierra Nevada during spring, when the  
 93 dust-in-snow largely influences snow albedo and snowmelt? We integrate models and observations to  
 94 understand how the dust deposition is linked to a specific source both surrounding and far from the Sierra  
 95 Nevada.

96

## 97 **2.1 Model and Reanalysis datasets**

### 98 **2.1.1 WRF-Chem configuration**

99 Table 1. Model configuration.

<b>Atmospheric processes</b>	<b>WRF-Chem Configuration</b>
Meteorological IC/LBCs	ERA5
Microphysics	Morrison double-moment
Radiation	RRTMG for both shortwave/longwave
Land surface	CLM4 with SNICAR
Surface layer	Revised MM5 Monin-Obukhov
Planetary boundary layer	YSU scheme
Cumulus	Grell-Freitas
Chemical driver	MOZART
Aerosol driver	MOSAIC 4-bin
Anthropogenic emission	NEI2017
Biogenic emission	MEGAN
Biomass burning emission	FINNv2.2

Dust emission	GOCART
Chemical IC/BC conditions	CAM-Chem

100  
101           We used the WRF-Chem version 3.9 to study dust emission and transport across the Sierra Nevada.  
102 The model setups (Table 1), including the physical schemes and emission inventory, follow Huang et al.  
103 (2022a), which showed that the model captures the distribution and variation in aerosols reasonably well in  
104 the study domain (126.12-112.86°W, 32.3-43.0°N). The Model of Ozone and Related chemical Tracers  
105 (MOZART) chemistry module (Emmons et al., 2020) and the Model for Simulating Aerosol Interactions  
106 and Chemistry with four bins (MOSAIC 4-bin) aerosol model (Zaveri and Peters, 1999) were applied, and  
107 dust emissions were calculated “online” using the GOCART dust scheme (Ginoux et al., 2001). The  
108 meteorological initial and lateral boundary conditions were derived from the ECMWF Reanalysis v5  
109 (ERA5) at 0.25° horizontal resolution and 6 h temporal intervals (Hersbach et al., 2020). Spectral nudging  
110 was employed with a timescale of 6 h above the PBL to reduce the drift between ERA5 reanalysis data and  
111 WRF’s internal tendencies (Von Storch et al., 2000). The chemical initial and boundary conditions were  
112 provided by CAM-Chem (Buchholz et al., 2019).

113           We applied the model to two nested domains (Fig. 1). Domain 1 (126.12-112.86°W, 32.3-43.0°N)  
114 was configured to cover all of California, Nevada, and part of the surrounding states with 110 × 120 grid  
115 cells at 10 km × 10 km horizontal resolution; the nested domain 2 covered the Sierra Nevada and  
116 surrounding regions with a 2 km × 2 km resolution. The cumulus scheme is turned off in domain 2 with  
117 convection-permitting resolution. We used 35 vertical model layers from the surface to 10 hPa with denser  
118 layers at lower altitudes to resolve the PBL. The simulation period ranged from September 20, 2018, to  
119 August 31, 2019 while we only used output from February to June in consideration of both dust emission  
120 season and mountain snow existence (Hand et al., 2016; Kim et al., 2021; Achakulwisut et al., 2017).

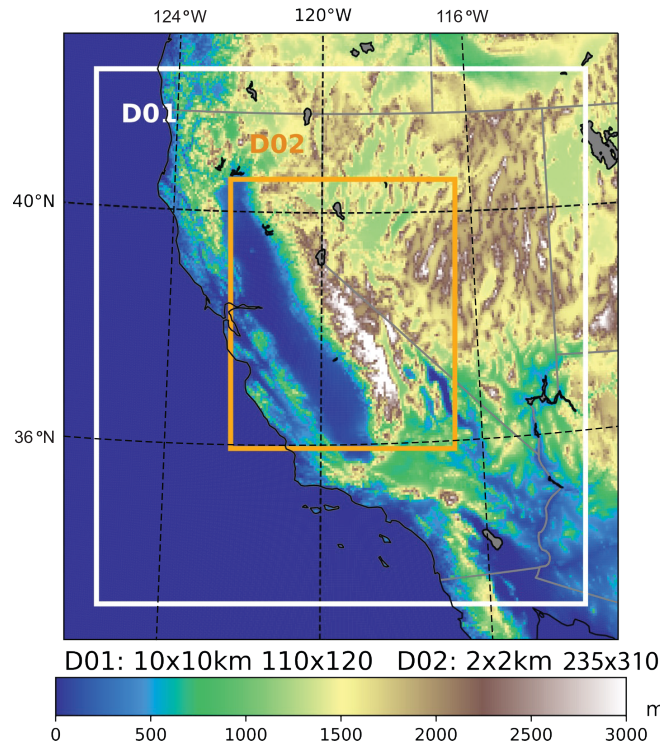


**Figure 1** WRF-Chem simulation domain 1 (D01) and domain 2 (D02) used in this study

121  
122  
123

## 124 2.1.2 MERRA-2 and ERA5 reanalysis

125 The Modern-Era Retrospective analysis for Research and Applications, Version 2 (MERRA-2) is  
 126 a widely used atmospheric reanalysis with a spatial resolution of  $0.500^{\circ} \times 0.625^{\circ}$  and 72 vertical layers  
 127 (Buchard et al., 2017). MERRA-2 aerosol products are produced by combining GEOS atmospheric model  
 128 version 5 (GEOS-5) with a 3D variational data assimilation algorithm to incorporate satellite observations,  
 129 including Advanced Very High Resolution Radiometer (AVHRR), Moderate Resolution Imaging  
 130 Spectroradiometer (MODIS), and Multi-angle Imaging Spectro Radiometer (MISR), as well as ground-  
 131 based observations such as the AERonet RObotic NETwork (AERONET) (Gelaro et al., 2017). Although  
 132 the aerosol vertical profile, composition, and size distributions are not constrained by the assimilation of  
 133 aerosol optical depth (AOD), previous studies demonstrated that the aerosol assimilation system has  
 134 considerably improved the agreement with numerous observed aerosol properties (Buchard et al., 2016;  
 135 Buchard et al., 2017; Randles et al., 2017). The assimilation results in the imbalance of global dust mass  
 136 and produces a considerably larger deposition than the simulated dust emission (Buchard et al., 2017).

137 MERRA-2 simulates dust with diameter bins of 0.2–2.0 (DU001), 2.0–3.6 (DU002), 3.6–6.0 (DU003), 6.0–  
138 12.0 (DU004), and 12.0–20.0 (DU005)  $\mu\text{m}$ , while the MOSAIC 4-bin in WRF-Chem simulates dust with  
139 geometric size bins of 0.039–0.156, 0.156–0.625, 0.625–2.5, and 2.5–10.0  $\mu\text{m}$ . We therefore use the dust  
140 concentrations of the first 4 size bins in MERRA-2 (DU001 + DU002 + DU003 + 0.74 \* DU004) to match  
141 with dust with geometric size less than 10.0  $\mu\text{m}$  in WRF-Chem  
142 (<https://gmao.gsfc.nasa.gov/reanalysis/MERRA-2/FAQ/>).

143 ERA5 provides assimilated wind fields at a  $0.25^\circ \times 0.25^\circ$  horizontal resolution at 137 hybrid  
144 sigma/pressure levels from 1979 to near real time (Hersbach et al., 2020). This study obtained the 3-hourly  
145 meridional and zonal wind field from February to June 2019 from 1000 to 500 hPa. The ERA5 wind  
146 reanalyses were used with satellite-retrieved dust optical depth (DOD) to evaluate the classified dust  
147 emission and transport patterns from the model.

148

## 149 **2.2 Satellite observations for validation**

150 The Infrared Atmospheric Sounding Interferometer (IASI) onboarded European Meteorological  
151 Operation (MetOp) satellite series measures infrared radiation in 8,461 spectral channels between 3.63 and  
152 15.5  $\mu\text{m}$ . The instrument provides near-global coverage with a spatial resolution of 12 km at nadir (Hilton  
153 et al., 2012) since 2007. IASI is primarily sensitive to coarse mode dust particles, and thus the retrieved  
154 AOD at the wavelength of 10  $\mu\text{m}$  can represent the DOD (Yu et al., 2019). Note that the thermal infrared  
155 (IR) AOD reported by IASI is usually significantly smaller than the visible AOD in MODIS, because of  
156 the spectral dependence of dust extinction (Zheng et al., 2022). We use the version 2.2 AOD product  
157 developed at the Centre National de la Recherche Scientifique Laboratoire de Météorologie Dynamique  
158 from <https://iasi.aeris-data.fr/dust-aod/> (February 2022) (Capelle et al., 2014). The  $0.3^\circ \times 0.3^\circ$  daily AOD  
159 data covering California were produced by aggregating day and night retrievals at the satellite pixel  
160 resolution (Capelle et al., 2018), in consideration of both data completeness and fine features. The  $1.0^\circ \times 1.0^\circ$   
161 daily AOD was produced in a similar way to investigate dust transport from Asia across the North Pacific.

162 The MIDAS (ModIs Dust AeroSol) dataset provides global fine-resolution ( $0.1^\circ \times 0.1^\circ$ ) daily DOD  
163 between 2003 and 2017 using quality-filtered AOD from MODIS Aqua and DOD-to-AOD ratios from  
164 MERRA-2 reanalyses (Gkikas et al., 2021). Despite the uncertainties in modeled DOD-to-AOD ratios, the  
165 validations of the MIDAS dataset against the AERONET dust-like AOD and the Lidar climatology of  
166 Vertical Aerosol Structure for space-based lidar simulation (LIVAS) DOD reveal a high level of agreement  
167 at both global and station level (Gkikas et al., 2022). Compared with other MODIS-derived DOD products  
168 (Song et al., 2021; Voss and Evan, 2020; Ginoux et al., 2012; Pu and Ginoux, 2018), MIDAS has finer  
169 spatial and temporal resolutions over both land and ocean, which is particularly applicable in this study  
170 focusing on a small region and a few cases at daily scale. The dataset has been extended to near real-time  
171 to match our study year.

172 Cloud-Aerosol Lidar with Orthogonal Polarization (CALIOP) is a two-wavelength (532 and 1064  
173 nm) polarization lidar onboarded the Cloud-Aerosol Lidar and Infrared Pathfinder Satellite Observation  
174 (CALIPSO) satellite (Hunt et al., 2009). Since June 2006, the lidar has been collecting an almost continuous  
175 record of high-resolution profiles of aerosol and clouds as fine as 30 m in the vertical, covering  $82^\circ\text{N}$  to  
176  $82^\circ\text{S}$  (Winker et al., 2010; Winker et al., 2009). This study used clear-sky data from the CALIOP Version  
177 4, level-2 aerosol profile product (Young et al., 2018) to investigate the vertical profile of elevated dust  
178 layer, especially from remote transport. When there were large DOD shown in IASI and MIDAS, we  
179 examined the vertical profiles of dust by identifying the “dust,” “polluted dust,” and “dusty marine” species  
180 in the CALIOP data (Kim et al., 2018)

181

### 182 **2.3 SOM analysis**

183 We applied the self-organizing map (SOM), a clustering method developed in the field of artificial  
184 neural networks, to recognize different weather features associated with dust transport and deposition..  
185 SOM has been widely used in atmospheric sciences to recognize spatially organized sets of patterns in the  
186 data (Reusch et al., 2007; Bao and Wallace, 2015; Liu et al., 2022; Song et al., 2019). Before the machine-  
187 learning process, Before the machine-learning process, we assign a few two-dimensional arrays of initial

188 nodes randomly or more efficiently from the leading empirical orthogonal functions (EOFs). During the  
189 training phase, the Euclidean distance between each input pattern and the initiation nodes is calculated to  
190 begin an iterative procedure. The best-matching node or the “winning” node is the one with the smallest  
191 distance between the initiation nodes and the input vector. Then the winning node and the neighborhood  
192 nodes around the winner are updated to adjust themselves toward the input vector. Since this process is  
193 iterated and fine-tuned, the nodes are self-organizing. The final SOM nodes represent typical dust transport  
194 and deposition patterns across the Sierra Nevada.

195         Here, we first used five variables from WRF-Chem inner domain (D02) in the SOM clustering,  
196 including dust deposition flux at the Sierra Nevada, the low-level meridional and zonal dust transport fluxes,  
197 and the mid-level meridional and zonal dust transport fluxes surrounding the Sierra Nevada. The original  
198 fields were used without any no filtering methods to consider the extreme cases. The 3 hourly model outputs  
199 during February-June 2019 are used to count for the spatial distribution and temporal evolution of dust  
200 transport and deposition. For WRF-Chem, we averaged the zonal and meridional dust fluxes in model levels  
201 3-5 (roughly 900-950 hPa over coastal California and 650-700 hPa over the Sierra Nevada) to acquire the  
202 low-level transport features. We averaged 200-700 hPa fluxes to acquire the mid-level transport features.  
203 Levels 3-5 were selected to focus on airborne particulate matter entrained above the planetary boundary  
204 layer and transported on the regional scale. Remote transport of Asian and African dust is mostly found  
205 around 600–200 hPa, which flows downward to the lower troposphere along the post-cold isentropic surface  
206 into the atmospheric river (AR) environment (Voss et al., 2021). By selecting levels between 200-700 hPa,  
207 we were able to include all cross-Pacific remote transport in the middle level.

208         We tested the number of clusters ( $k$ ) that ranges in 3, 4, 5, 6, 8, 9, and 16 to assess the distinctiveness  
209 and robustness of different  $k$ . For each  $k$ , the robustness of the clusters was measured by a classifiability  
210 index (CI) (Vigaud and Robertson, 2017; Vigaud et al., 2018; Hannachi, 2010) constructed using the  
211 minimum spatial correlation coefficient between the clusters obtained from the full data and many random  
212 halves of the data (100 halves used here) (Hannachi, 2010). Therefore, the CI measured the reproductivity  
213 of the  $k$  clusters partitioning (Visbeck et al., 2001), with perfect partitioning leading to 1. Figure S1 shows

214 the CI as a function of the number of clusters using WRF-Chem output for 2019. With the highest CI, the  
215 4-cluster partitioning well represents distinct dust transport and deposition patterns over the Sierra Nevada  
216 and is used in this study.

217 To verify the recognized transport patterns based on WRF-Chem, we conducted SOM analyses  
218 using variables from MERRA-2. We first remapped the same five variables using bilinear interpolation  
219 from  $0.5^\circ \times 0.625^\circ$  to 10 km, the resolution of the WRF-Chem outer domain, before clustering. The vertical  
220 levels of low-level and mid-level dust transport fluxes were selected to approximately match the WRF-  
221 Chem pressure level. Four nodes were identified and arranged to make a direct comparison with those from  
222 WRF-Chem. To further investigate if transport patterns recognized from SOM vary significantly with years,  
223 we applied SOM analyses over 2001-2021 using MERRA-2 extended records of dust fluxes and deposition.

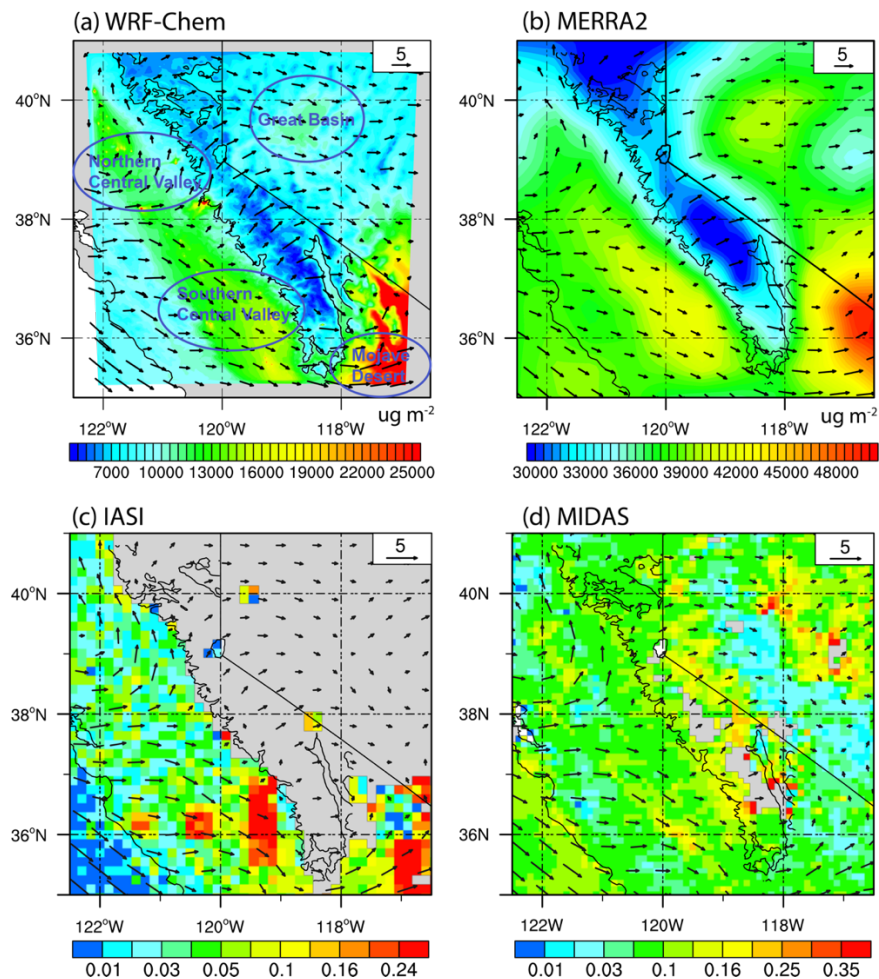
224

### 225 **3. Results**

#### 226 **3.1 Dust emission sources around the Sierra Nevada**

227 We find four emission source regions surrounding the Sierra Nevada where dust emissions could  
228 potentially influence the mountain snow impurities between February and June (Fig. 2). The Mojave Desert,  
229 located southeast of the Sierra Nevada, is characterized by low annual precipitation, sparse vegetation, and  
230 dried fine soil. Airborne dust loading over the desert can reach  $30000 \text{ ug m}^{-2}$  averaged over our study period  
231 (Fig. 2a). It is generally transported eastward but can also be transported westward, influencing the southern  
232 part of the mountain (Neff et al., 2008). Dust produced in the northern (Sacramento Valley) and the southern  
233 part (San Joaquin and Tulare Basins) of the Central Valley is often transported eastward to the mountains.  
234 With high soil aridity and a higher fraction of dry sand (Duniway et al., 2019), the southern Central Valley  
235 is more erodible and emits a higher amount of fine dust. The Great Basin dust is relatively weak in  
236 magnitude but located at a higher altitude. Therefore, it can easily ride along wind currents upward along  
237 the east slope of the mountain. The column dust loading in MERRA-2 confirms our results in WRF-Chem  
238 (Fig. 2b), despite it showing a stronger dust emission in the Great Basin while a weaker one in the  
239 Sacramento Valley. The IASI shows the strongest IR DOD in the Mojave Desert, followed by the southern

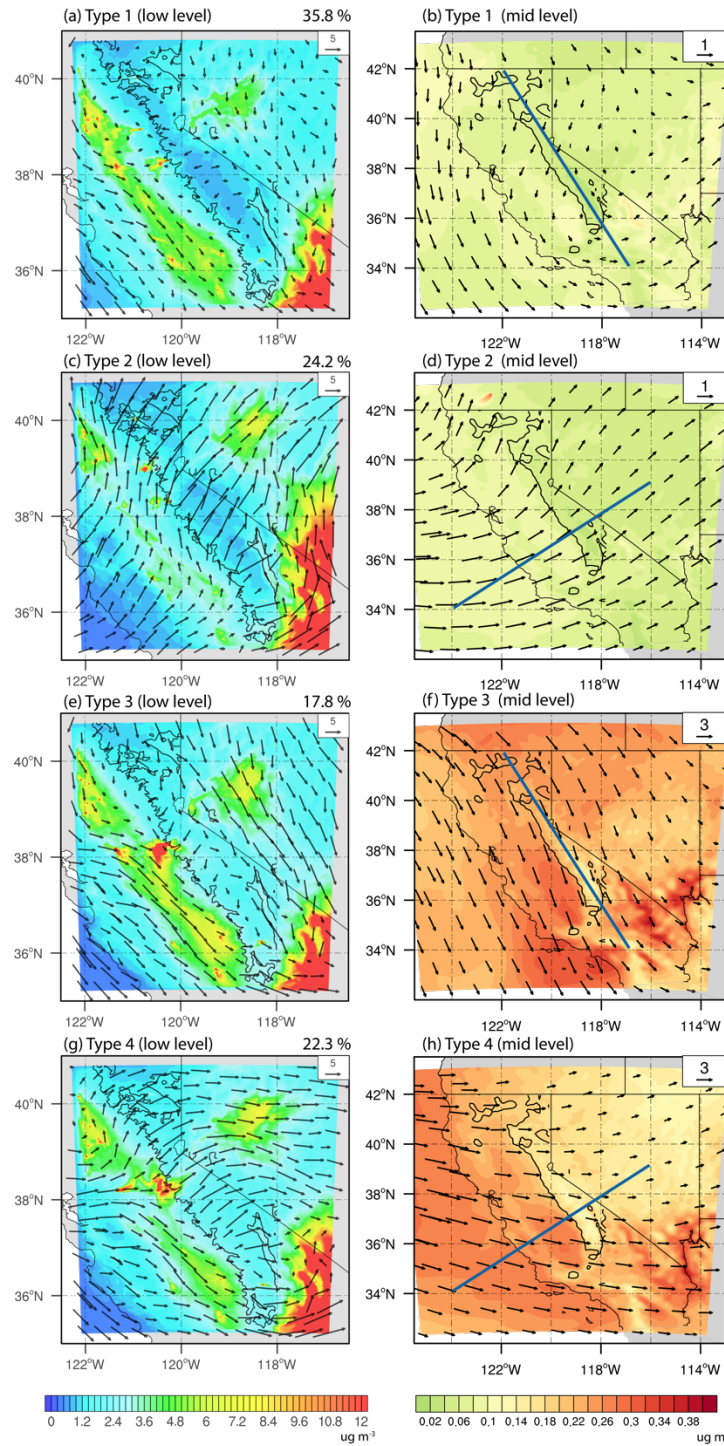
240 Central Valley, but smaller dust emissions from the Sacramento Valley as compared with model output  
 241 (Fig. 2c). The smaller magnitude is largely due to the fact that IASI measures the radiation at IR  
 242 wavelengths, which is more sensitive to coarse-mode dust particles (Yu et al., 2019), whereas the fine dust  
 243 produced in the Central Valley has a negligible contribution to DOD at 10  $\mu\text{m}$ . In contrast, MIDAS captures  
 244 dust emissions from the Great Basin, the southern and northern Central Valley (Fig. 2d) but not the Mojave  
 245 Desert. MIDAS is reported to underestimate DOD from the Mojave Desert compared to AERONET DOD,  
 246 which might be caused by the lower dust amounts simulated in MERRA-2 (Gkikas et al., 2021) and the  
 247 underestimation of MODIS AOD over the deserts as compared to ground observations (Tao et al., 2017).



248  
 249 **Figure 2** The spatial distribution of dust in model and satellite observations averaged in 2019 February-  
 250 June. Column dust loading ( $\text{ug m}^{-2}$ ) and low-level winds (roughly 875-925 hPa;  $\text{m s}^{-1}$ ) in (a) WRF-Chem  
 251 and (b) MERRA-2. (c) Observed thermal infrared DOD at the wavelength of 10  $\mu\text{m}$  from IASI (d) Observed  
 252 visible DOD at the wavelength of 550  $\mu\text{m}$  from MIDAS. The low-level winds ( $\text{m s}^{-1}$ ) in (c) and (d) are from  
 253 ERA5 reanalyses. Black contours indicate the elevation of 1500 m, which represents the Sierra Nevada  
 254 range used in this study. The grey area in c-d are missing pixels in satellite observations



256 **3.2 Dust transport across the Sierra Nevada**



257  
258  
259  
260  
261

**Figure 3** (a, c, e, g) Low-level (roughly 875-925 hPa) dust concentration ( $\mu\text{g m}^{-3}$ ) and wind vectors ( $\text{m s}^{-1}$ ) in each of the four SOM type in WRF-Chem; The numbers on the top right of subplots denote the frequency of each type. (b, d, f, h) Mid-level (200-700 hPa average) dust concentration ( $\mu\text{g m}^{-3}$ ) and dust transport in types 1-4; The position of the cross-section used for Figure 5 is denoted in each plot.

262

263

264

265

266

267

268

269

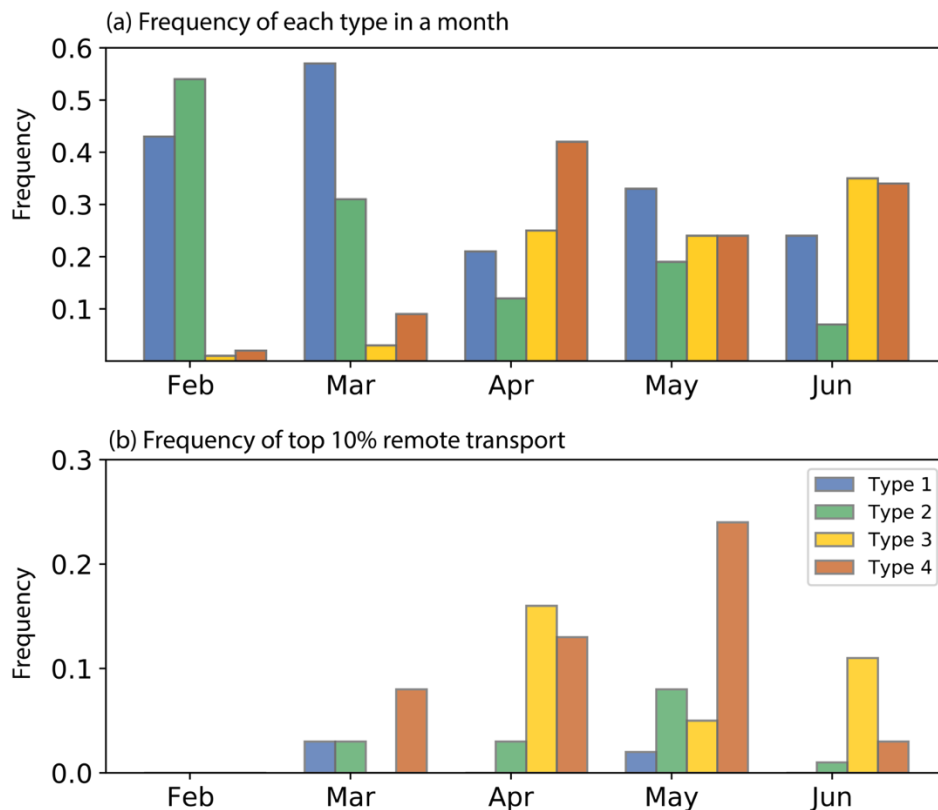
270

271

272

This section introduces the features of dust transport patterns discerned from WRF-Chem and evaluates them against satellite observations over the period of February to June 2019. Figure 3 shows the WRF-Chem dust concentration and wind in the low levels and middle levels averaged for each of the four types acquired from the SOM analyses. The dust transport pattern represented in SOM type 1 accounts for 35.8% of hours from February to June (Fig. 3a), especially in February (43%) and March (57%) (Fig. 4a). Type 2 occurs in 24.2% of the whole study period and contributes to more than 50% in February and then decreases with the month. In contrast, types 3 and 4 account for 17.8% and 22.3%, respectively, with the occurrence increasing with the month. The maximum occurrence is found in June for type 3 (40%) and April for type 4 (34%), respectively.

### 3.2.1 Mesoscale regional (MSR) transport



273

274

275

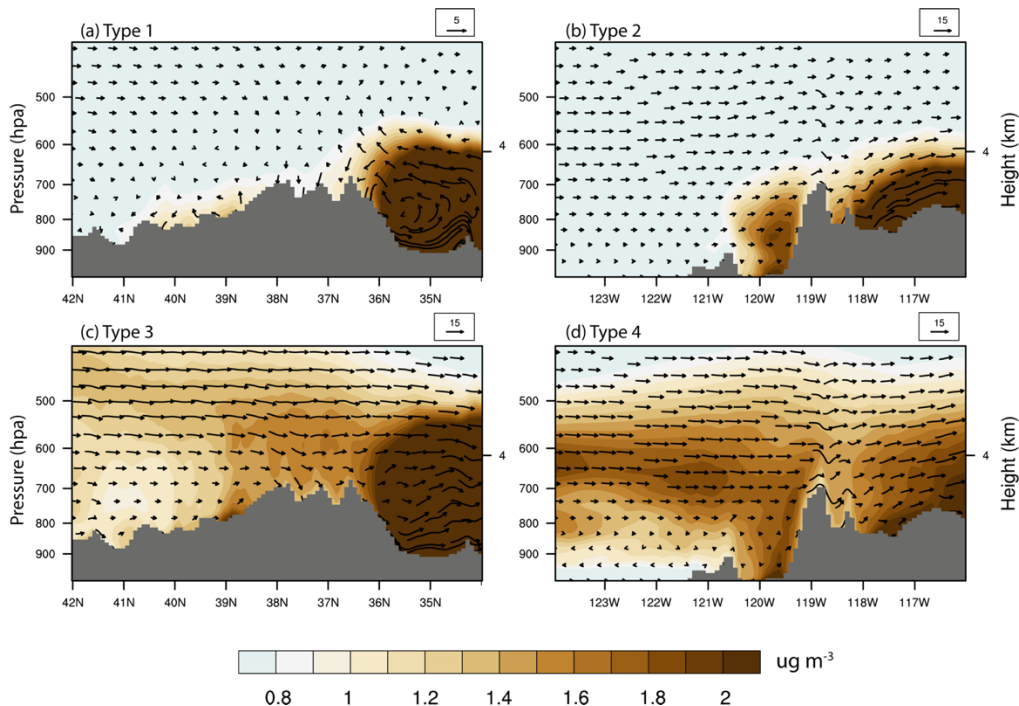
276

277

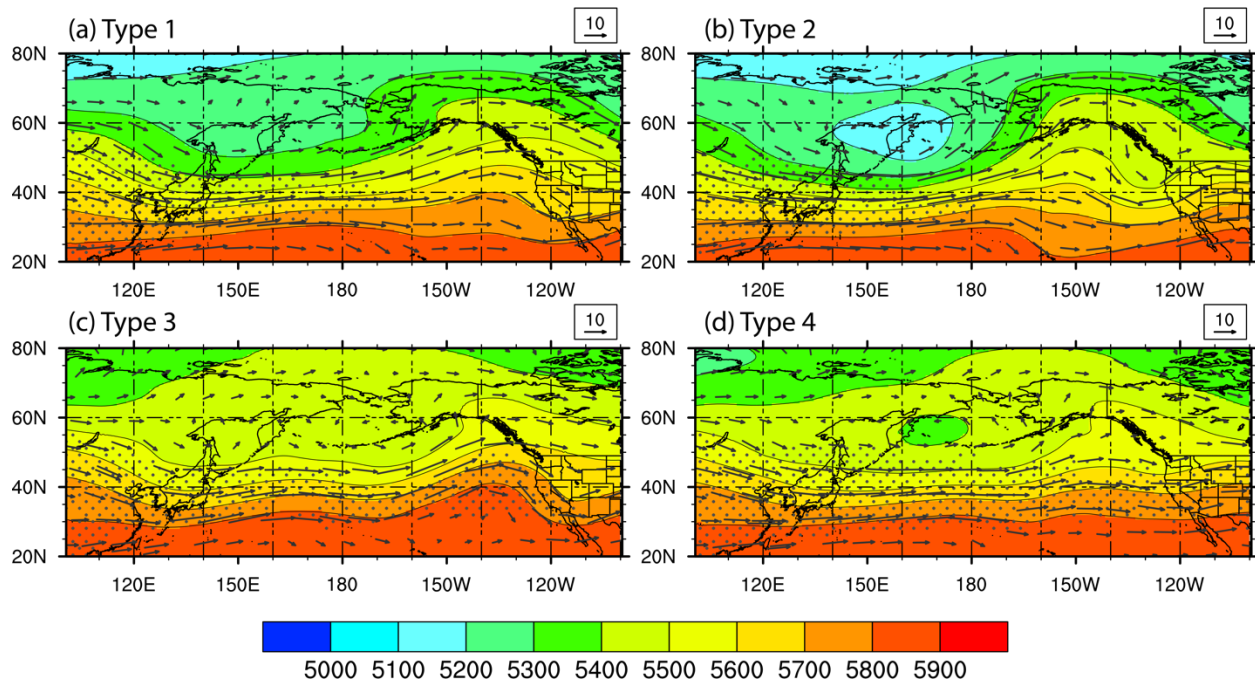
278

**Figure 4** (a) The frequency of each type (the time dominated by each type divided by total time in a month) that occurs in February, March, April, May, and June in WRF-Chem. (b) The frequency of each type in the top 10% remote transport (the time dominated by each type divided by total time of the top 10% remote transport).

279 In type 1, dust is transported from northwest to southeast in the Central Valley in the low level  
 280 (roughly 875-925 hPa over the California coast). A vortex (Schultz Eddy) was found in the northern Central  
 281 Valley (Fig. 3a), circulating counter-clockwise and confining dust to the local environment (Bao et al.,  
 282 2008). The air inflow from the ocean is relatively weak and obstructed by the terrain. The Great Basin is  
 283 dominated by the northwesterlies. The emitted dust is transported southeastward and blocked by the  
 284 mountain, depositing dust on the east slope. Dust emitted from the Mojave Desert can be elevated to the  
 285 middle level (Fig. 3b). The cross-section further shows a vertical circulation where the Mojave Desert dust  
 286 is blown away from the Sierra Nevada at the low level and towards the mountain at 600-700 hPa (Fig. 5a).  
 287 A weaker mid-level cross-Pacific flow is found in type 1 than in other types (Fig. 6a), with no signals of  
 288 remote transport reaching the Sierra Nevada (Fig. 3b). Type 1 generally corresponds to the dust transport  
 289 in lack of prevailing large-scale weather systems. The high peaks of the Sierra Nevada produce mesoscale  
 290 circulations and prevent the Central Valley and Great Basin dust from being transported to the other side  
 291 of the mountain. It is referred to as the “mesoscale regional (MSR) transport” hereafter.



292 **Figure 5** Cross-section of dust concentration (shaded;  $\text{ug m}^{-3}$ ) and dust transport fluxes (vectors;  $\text{ug m}^{-2} \text{s}^{-1}$ )  
 293 at 1000-400 hPa for each SOM type in WRF-Chem. The position of each cross-section is denoted in Fig.  
 294 3 b (Type 1), d (Type 2), f (Type 3), and h (Type 4). The grey area indicates the topography of the Sierra  
 295 Nevada.  
 296

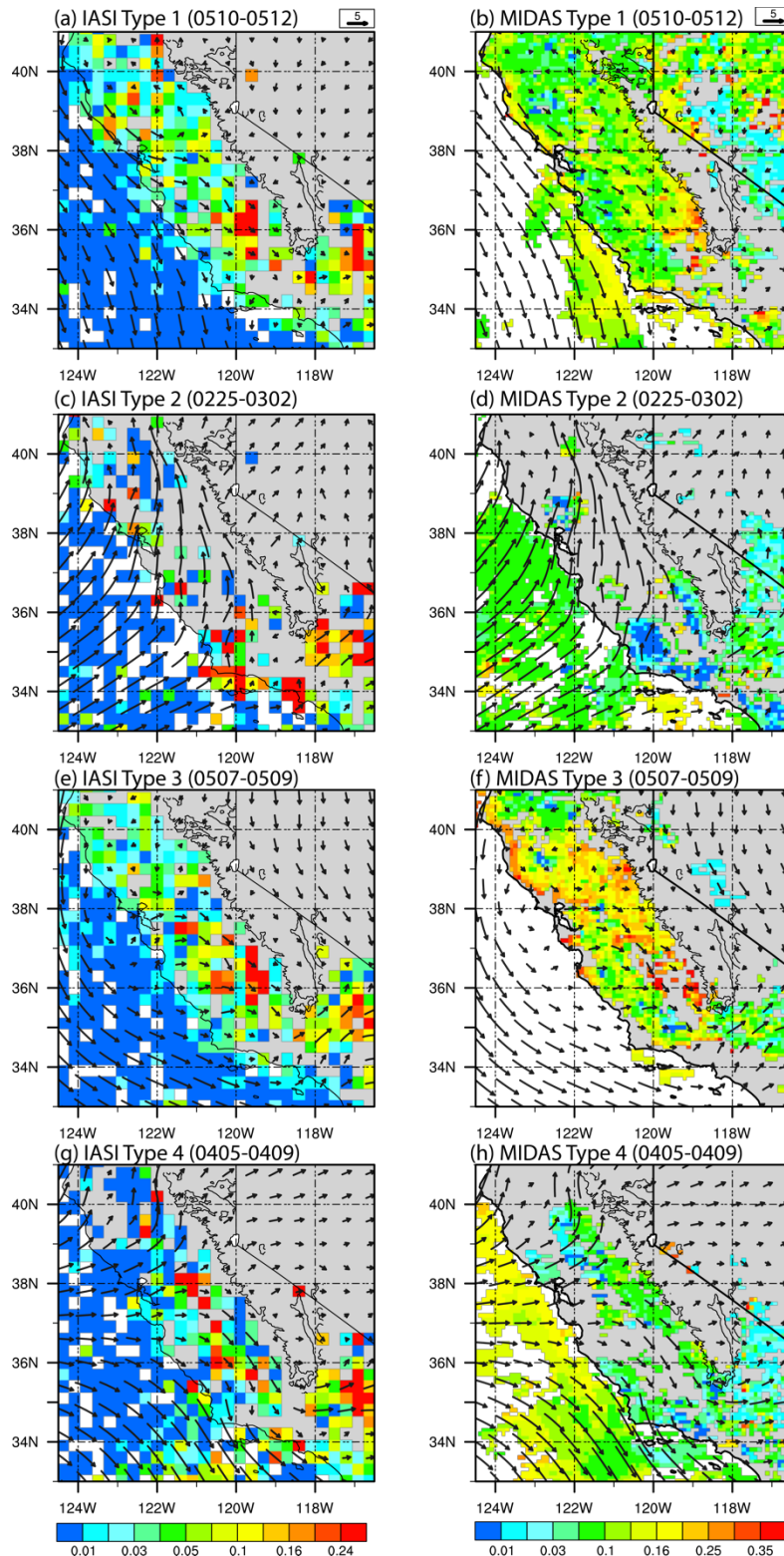


297

298 **Figure 6** Geopotential height (gpm) and wind vectors ( $\text{m s}^{-1}$ ) at 500 hPa in each of the four SOM types in  
 299 WRF-Chem. The dotted regions indicate DOD higher than 0.03 from MERRA-2  
 300

301 We validate the features of type 1 from WRF-Chem using satellite retrieved DOD and wind vectors  
 302 from ERA5. The cloud contamination results in many missing satellite pixels in our study domain, making  
 303 the transport patterns hard to discern on a single day. DOD and winds belonging to the same SOM type on  
 304 consecutive days are averaged to maximize the data completeness. One typical example for each type is  
 305 presented based on their representativeness and the maximum spatial coverage. Figures 7a-b present dust  
 306 emission and transport patterns during May 10-12, a typical case for the MSR transport. In IASI, we find  
 307 peak IR DOD ( $> 0.2$ ) over the Mojave Desert and the southern Central Valley and moderate values in the  
 308 Sacramento Basin related to the Schultz Eddy (Fig. 5a), resembling the relative magnitude of dust  
 309 concentrations in regional source regions in WRF-Chem (Fig. 3a). MIDAS shows another evidence of dust  
 310 transport pathways within the Central Valley with a higher resolution, although the maximum DOD shifts  
 311 slightly towards the mountain range (Fig. 7b). Dust emissions from the Great Basin are weaker than those  
 312 from the southern Central Valley.





313  
 314 **Figure 7** (a,c,e,g) IR DOD at the wavelength of 10  $\mu\text{m}$  retrieved from IASI and (b,d,f,h) visible DOD at  
 315 the wavelength of 550  $\mu\text{m}$  from MIDAS for each type. The low-level winds (vectors;  $\text{m s}^{-1}$ ) are obtained  
 316 from the ERA5 reanalyses. The numbers in the parenthesis indicate the event time period for the year 2019.  
 317

318 **3.2.2 Sierra-barrier-jets-related (SBJ-related) transport**

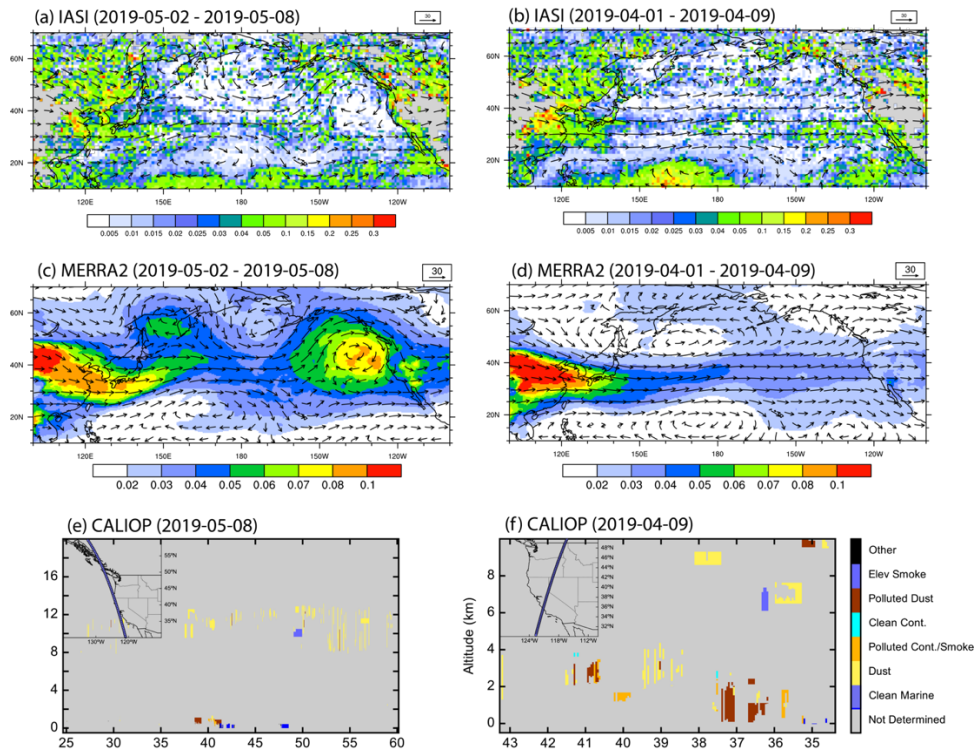
319 In type 2, the low-level winds turn to the north above the western slope of the Sierra Nevada (Fig.  
320 3c), which resembles the terrain-locked Sierra barrier jets (SBJs) typically observed during the presence of  
321 ARs (Neiman et al., 2013). The large-scale pattern consists of a low 500hPa geopotential height (GPH)  
322 center in the north Pacific (Fig. 6b). The meridional gradient produces intense storm tracks from Kuroshio  
323 Current towards Alaska (Rodionov et al., 2007). Indeed, we find extensive precipitations in type 2 (not  
324 shown), which produce more wet deposition along the mountain's windward (west and south-facing) slopes  
325 and result in cleaner air in the Central Valley (Fig. 3c). The dust layer at the Central Valley is found below  
326 700 hPa, mostly blocked by the high mountain peaks and is hardly transported to the lee-side (east) slope  
327 of the mountain (Fig. 5b), despite the cross-barrier westerlies found in the middle level. Dominated by SBJs,  
328 dust generated in the Great Basin and the Mojave Desert is blown away from the mountain. No clear signal  
329 of remote transport is found on the California coast (Fig. 3d). The dust transport from all sources is closely  
330 connected to SBJ; therefore, type 2 is referred to as the "SBJ-related" transport. In both IASI and MIDAS,  
331 we find more missing pixels for SBJ-related transport than any other type caused by cloud contamination  
332 (Figs. 7c-d). The AR-related landfalling precipitations from February 25 to March 2 remove the airborne  
333 dust particles. A cleaner atmosphere might be induced, but it is hard to confirm considering the missing  
334 pixels over the continent.

### 335 **3.2.3 North-Pacific-High-related (NPH-related) transport**

336 Type 3 has northwestern winds in both Central Valley and the Great Basin (Fig. 3e), transporting  
337 Central Valley dust to the southwest part of the Sierra Nevada in early summer. It is known as the "North-  
338 Pacific-High-related (NPH-related)" transport, during which the North Pacific High (NPH) built up in the  
339 north Pacific 130° W produces the northwest-southeast wind direction along the California coast (Fig. 6c),  
340 influencing the transport patterns for dust emitted from the surrounding sources. At the middle level, we  
341 observe a meridional mid-level dust transport pathway (Fig. 3f), which appears at 400-500 hPa in the  
342 northern Sierra Nevada and descends to 700 hPa at 36-37 °N, the top of the southern Sierra Nevada (Fig.  
343 5c). "The MERRA-2 reanalysis DOD (Fig. 6c) further shows dust originating from Asia is transported

344 towards North America following the isobars and wind patterns (discussed further in section 3.2.3). The  
345 dust emitted from the Great basin is transported by the southward winds to the east slope of the mountains,  
346 while emissions from the Mojave Desert are transported away from the mountain range.

347         The simulated dust concentration and transport in the NPH-related transport are confirmed by DOD  
348 observations during May 7-9, with the transport pathway parallel to the California coast (Figs. 7e-f). Studies  
349 have shown two main pathways of Asian dust transport to North America during the spring months: (1)  
350 meridional excursions north into Alaska and then south along the U.S. west coast, and (2) zonal transport  
351 over the North Pacific Ocean (Creamean et al., 2014). With north-south dust transport at the middle level,  
352 the NPH-related transport characterizes the first pathway. To examine this hypothesis, we averaged the IR  
353 DOD and 500 hPa wind field over the North Pacific during May 2-9. We included a few days before the  
354 event (Fig. 8a) as it takes 7-10 days for dust to be transported from Asia to North America (Ault et al., 2011;  
355 Creamean et al., 2013). The dust transport pathway shows that after being emitted from East Asia and the  
356 Gobi Desert, dust is transported zonally to 150 °W, excursing north into Alaska/Canada and then traveling  
357 south along the U.S. west coast. Similar conclusions can be drawn with more evident pathways using DOD  
358 from MERRA-2 reanalyses (Fig. 8e). An elevated dust belt from 8 km to 12 km is discerned over the North  
359 American coast (27 °N to 60 °N) from the CALIOP data, denoting the north-south transport of a thin dust  
360 layer through the middle level (Fig. 8c).



361 Figure 8 (a) IR DOD from IASI and 500 hPa winds ( $\text{m s}^{-1}$ ) from ERA5 over the North Pacific for a typical  
 362 Type 3 case averaged between 2019-05-02 to 2019-05-08; (b) same as (a) but for a typical type 4 event  
 363 averaged between 2019-04-01 to 2019-04-09; (c) DOD from MERRA-2 and 500 hPa winds ( $\text{m s}^{-1}$ ) from  
 364 ERA5 for a 3 event; (d) same as (c) but for a type 4 event; (e) latitude-height cross-section of aerosol species  
 365 from CALIOP on 2019-05-08 (Type 3); (f) same as (e) but for a typical Type 4 case on 2019-04-09  
 366

367

### 368 3.2.4 Cross-Pacific zonal (CPZ) transport

369 Air inflows from the ocean enter California and diverge to the northern and southern branches in  
 370 type 4, transporting dust eastward across the Sierra Nevada (Fig. 3g). At the middle level, the low-GPH  
 371 center recedes in April, and the isobars become straighter than in boreal winter, which facilitates the zonal  
 372 transport of dust emitted from middle Asia over the North Pacific Ocean (Fig. 6d). The cross-section further  
 373 shows an elevated dust layer is transported from the ocean at around 700-500 hPa (Fig. 5d). The  
 374 concentrations are much stronger, and the altitude also lower than the NPH-related transport (Fig. 5c). The  
 375 remotely transported dust descends to low altitudes when reaching the California coast and converges with  
 376 the dust from the Central Valley at around 800 hPa. A portion of dust is compacted to the windward slopes  
 377 at higher elevations, and the remaining across the mountains affects the east slope. Dust emitted from the



378 Great Basin and the Mojave Desert is transported away from the mountains. Type 4 is denoted with “cross-  
379 Pacific zonal (CPZ) transport” to reflect the strong cross-Pacific dust transport.

380 April 5-9, a typical case for the CPZ transport, clearly shows the north and south branches of dust  
381 transport over the Central Valley (Figs. 7g-h). Different from the NPH-related transport pathway, the large-  
382 scale DOD and winds at 500 hPa (averaged over April 1-9) show that dust emitted from East Asia is being  
383 transported eastward, with a belt of IR DOD  $> 0.1$  evident around 25-40 °N (Fig. 8b). The DOD from  
384 MERRA-2 confirms the zonal pathways of dust transport with a smaller magnitude (Fig. 8d). The vertical  
385 distribution shows an elevated dust layer at 2-4 km above ground level, reaching the higher elevation of the  
386 mountain (Fig. 8f).

387 We calculated the mid-level dust remote transport, defined as the dust influxes from the north and  
388 west boundaries of the 200-700 hPa of WRF-Chem modeling domain 1, and investigated how the top 10%  
389 largest remote transport distribute in each SOM (Fig. 4b). Among all the large remote transport, CPZ  
390 transport accounts for 48% while NPH-related accounts for 32%, indicating that the zonal pathway plays a  
391 more important role in the cross-Pacific transport. Most remote transports are found in April and May, the  
392 former dominated by the meridional transport in the existence of the NPH while the latter led by the CPZ  
393 transport. The remaining two types contribute to a fairly small portion consistent with the clean atmosphere  
394 in the middle levels (Figs. 3b, d).

395

### 396 **3.2.5 Dust emissions and transport in back trajectory analyses**

397 We discern four types of dust transport patterns across the Sierra Nevada using the SOM clustering  
398 method. The MSR transport represents the local dust transport, which contributes to more than 20% of the  
399 time each month during February-June (Fig. 4a) in the absence of prevailing weather systems. The SBJ-  
400 related air inflows transport dust eastward and are closely related to the AR, during which the GPH and  
401 storm tracks at 500 hPa feature a typical large-scale pattern during the boreal winter (Rodionov et al., 2007).  
402 As time evolves, the GPH center recedes, and the isobars become more straight zonally in April, bringing  
403 dust from Asia and Africa to the western U.S. coast (CPZ transport). In early summer, the buildup of NPH

404 in the east Pacific corresponds to north-south winds along the California coast, transporting dust along the  
405 Sierra Nevada (NPH-related transport).

406 We further conducted air mass back trajectory (AMBT) simulations to evaluate the dust emission  
407 sources and transport pathways identified using SOM analyses. The back trajectory simulation was  
408 conducted using Hybrid Single-Particle Lagrangian Integrated Trajectory (HYSPPLIT) model with  
409 meteorological forcings from North American Mesoscale Forecast System. We selected typical days for  
410 the four SOM types as in Figure 7 and three sites located at the Central Sierra Nevada (38 °N, 120.3°W),  
411 Southern Sierra Nevada (36.5 °N, 119 °W), and Eastern Sierra Nevada (37 °N, 117 °W), to represent dust  
412 deposition at different subregions.

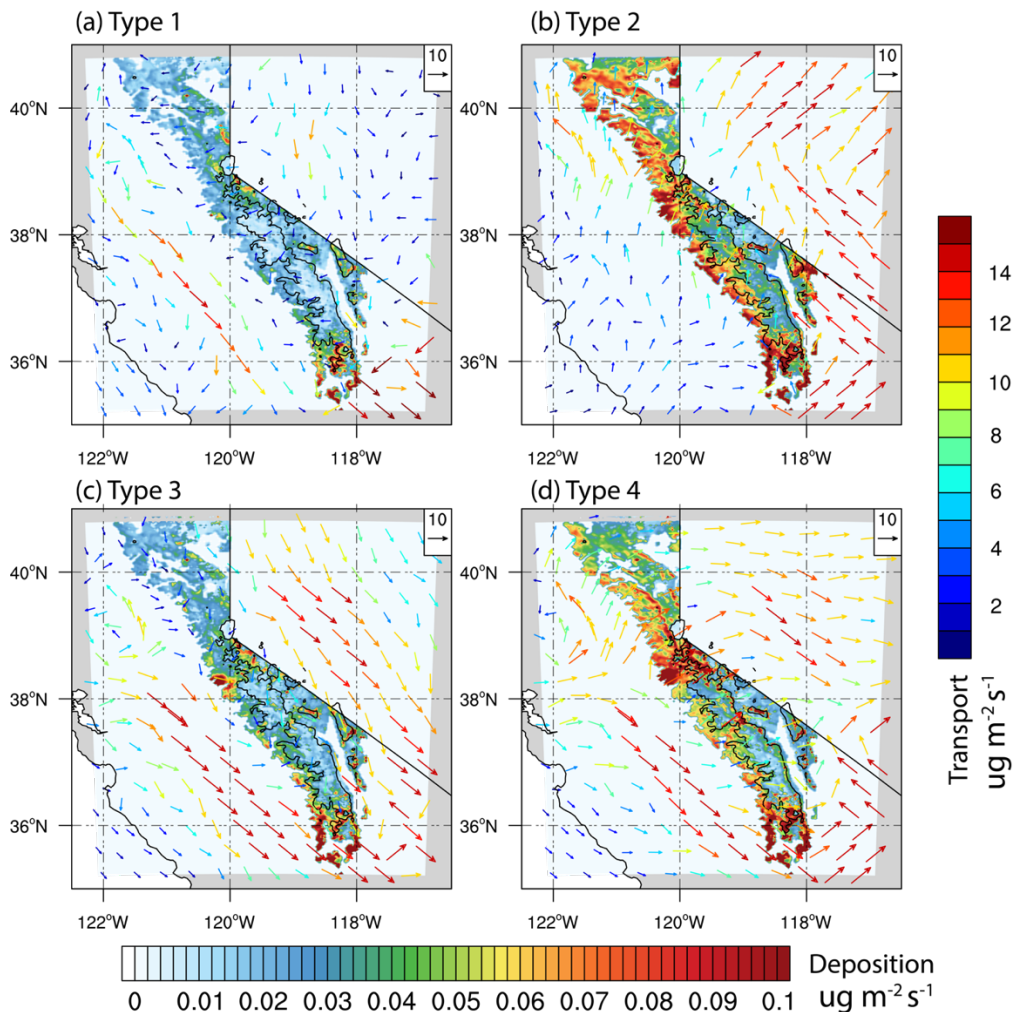
413 The results of 12-hour and 7-day AMBT results corroborate the identified local and long-range  
414 transport pathways for each type. The transport pathways generally follow the wind directions shown in  
415 Figure 7. Multiple emission source regions are found in type 1, including the Central Valley where dust is  
416 transported eastward to the windward slopes and the Great Basin where dust is transported westward to the  
417 lee-side slopes (Fig. S2). In type 2, dust deposited in all three sites comes from the Central Valley (Fig. S2),  
418 and the transport corresponds to the direction of SBJ during AR (Fig. 7c). Types 3 and 4 are affected by  
419 both local and remote transport. Locally, Dust mainly comes from the northern California and the Great  
420 Basin in type 3, while it comes from the Central Valley in type 4. Remotely, in type 3, we find dust emitted  
421 from Asia and North Africa excurses meridionally to Alaska at 135° W and then travels southward along  
422 the U.S. West Coast (Fig. S3a). In contrast, dust emitted from east Asia is transported zonally across the  
423 Pacific, reaching the Sierra Nevada from the west (Fig. S3b).

### 424 **3.3 Dust deposition over the Sierra Nevada**

425 The averaged dust deposition and low-level dust transport for each type are shown in Fig. 9, including  
426 both dry and wet depositions. The dry depositions consider the diffusion and gravitational effects, while  
427 wet depositions describe in-cloud removal (rainout) and below-cloud removal (washout) by grid-resolved  
428 stratiform precipitation as well as the sub-grid wet scavenging (Chapman et al., 2009; Easter et al., 2004).

429 In all SOM types, extensive depositions are found on the west slope in all types, generally decreasing with  
 430 elevation.

431 The MSR transport has the smallest deposition among the four types (Fig. 9a). Large depositions are  
 432 found in the southern Sierra Nevada and Lake Tahoe. Dust contributing to the deposition originates mainly  
 433 from the Mojave Desert and the Great Basin dryland. In contrast, large depositions found in the southern  
 434 and eastern parts of the mountains in NPH-related transport may be produced in agricultural land from the  
 435 southern Central Valley, as we find a persistent eastward transport pathway in the low level (Fig. 9c). The  
 436 remote transported dust plays a minor role as it is located above 8 km in altitude.



437  
 438 **Figure 9** (a-d) Dust deposition (shaded;  $\mu\text{g m}^{-2} \text{s}^{-1}$ ) over the Sierra Nevada and low-level dust transport  
 439 fluxes (colored vectors;  $\mu\text{g m}^{-2} \text{s}^{-1}$ ) across the Sierra Nevada averaged over each of the four SOM types in  
 440 WRF-Chem. Black contours indicate an elevation of 2500 m. The bottom color bar shows the magnitude  
 441 of dust deposition over the Sierra Nevada while the right color bar shows the magnitude of dust transport  
 442 flux vectors.

443

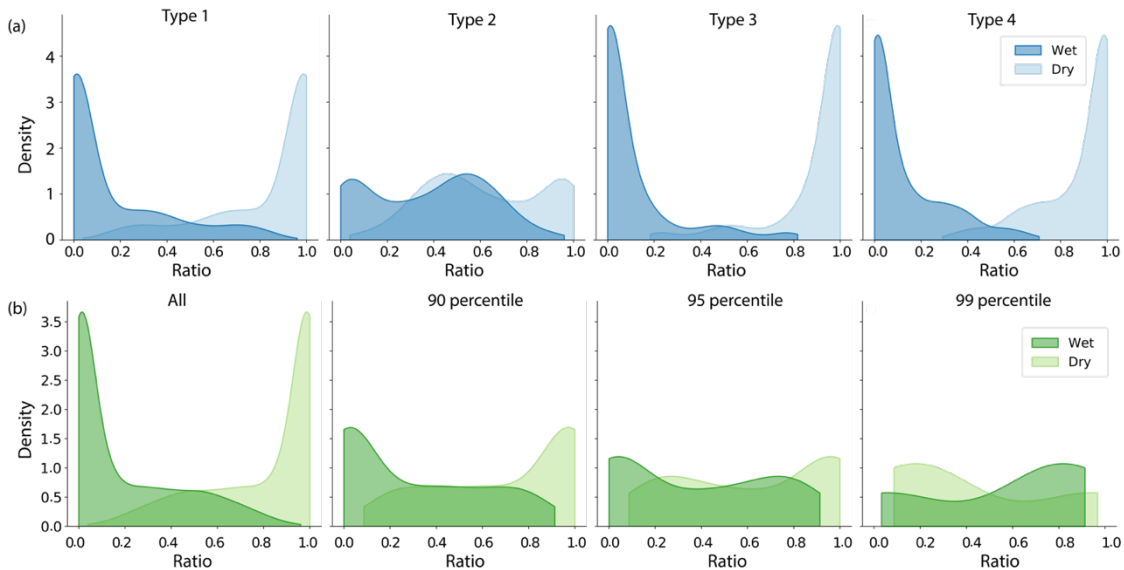
444 While SBJ-related transport has the lowest low-level dust concentration over the Central Valley, it  
445 produces the largest deposition along the west slope (Fig. 9b). Most eastward transport in the southern  
446 Sierra Nevada is obstructed by the high mountain peaks, resulting in large depositions below 2900 m. The  
447 SBJ turns eastward in the Sacramento Basins and climbs through the mountain north of 38 °N, producing  
448 a relatively homogenous deposition in the northern part. The combination of dust transport and deposition  
449 indicates that dust influencing the mountain snow impurities mostly comes from the Central Valley.  
450 Compared with the other SOM types, SBJ-related transport has large depositions at elevations higher than  
451 2500 m (discuss later). Large depositions are also found in the CPZ transport (Fig. 9d), with the largest  
452 value occurring on the west slope of the central and southern Sierra Nevada, contributed by both Asian dust  
453 and Central Valley dust. Compared to the MSR and NPH-related transport, the large-scale westerlies in the  
454 Central Valley (SBJ-related and cross-Pacific transport) produce larger deposition, probably because of the  
455 more efficient removal of particles by collision with terrestrial surfaces at higher elevations (Fig. 5d).

456 To quantify the relative importance of wet and dry depositions in each 3 hourly total deposition data,  
457 we calculate the fraction of wet depositions to total depositions averaged over the Sierra Nevada:

458  $\frac{Wet\ deposition}{Wet\ deposition + Dry\ deposition}$ . The contribution of dry deposition is defined in a similar way. We find the

459 wet deposition accounting for 40% in frequency in the SBJ-related type. The landfalling precipitation has  
460 deposited large amounts of airborne dust on the snow surface, producing a cleaner atmosphere as we have  
461 found in Fig. 3c. The frequent wet depositions also explain the larger depositions in high elevations (Fig.  
462 9b): dust particles reaching the high mountains are small in size and difficult to deposit through gravitational  
463 effects. Wet deposition is a more efficient way of depositing small particles as they collect dust in raindrops.  
464 In contrast, the dry depositions play predominant roles (more than 80% in frequency) in all the other types  
465 (Fig. 10a). Figure 10b further shows the contribution of wet deposition increases with deposition intensity.  
466 The averaged contribution of wet depositions in magnitude increases from 19% in all events to 29% in the

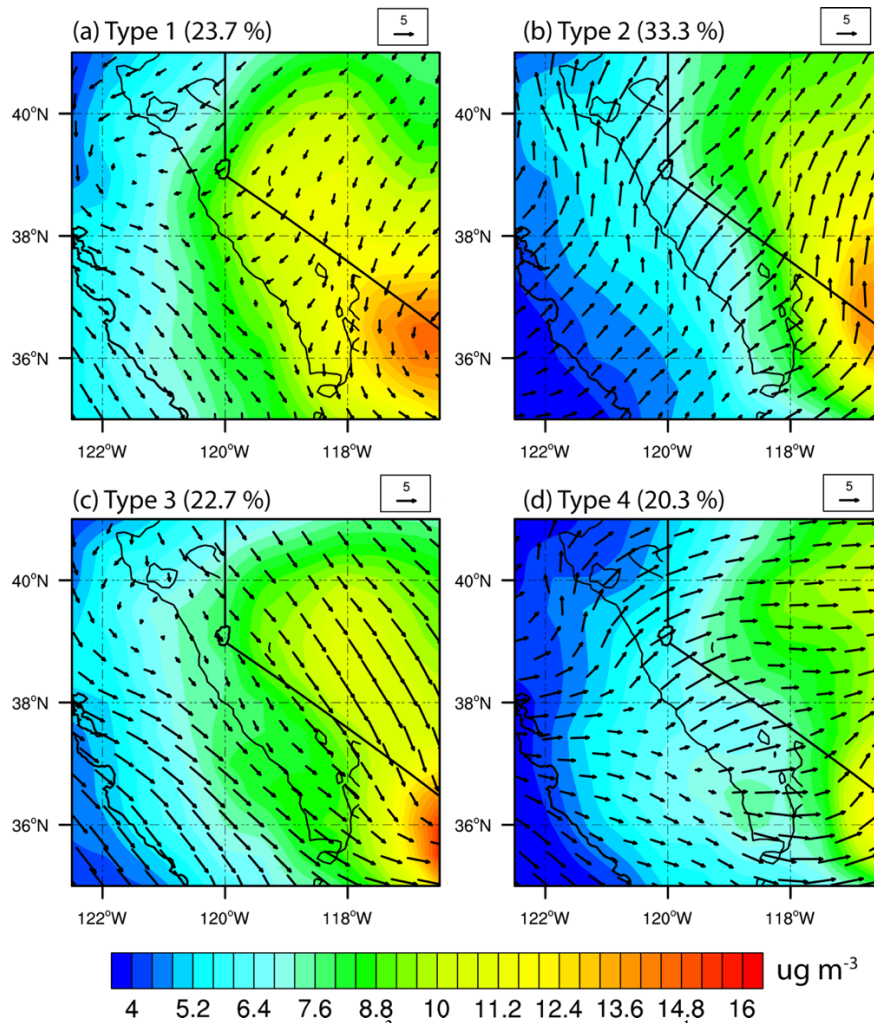
467 top 10 percentile, 36% in the top 5 percentile, and 56% in the top 1 percentile largest events, supporting  
468 our conclusion that wet deposition is a more efficient way of dust deposition.



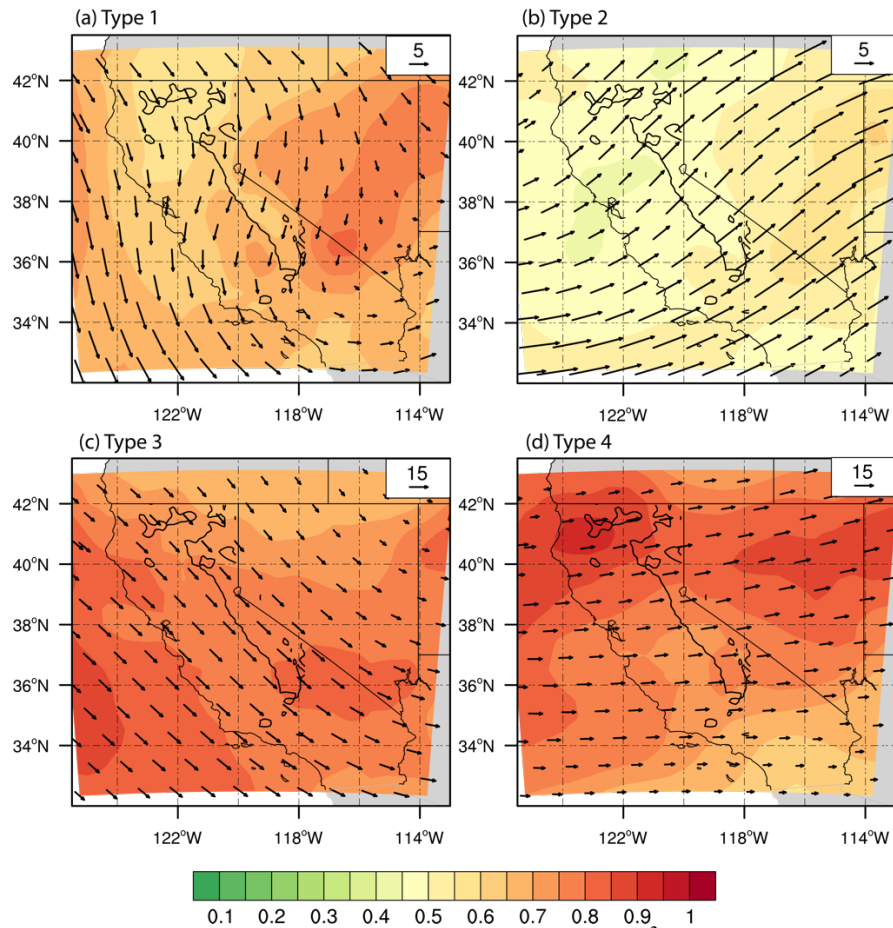
469 **Figure 10** (a) Distribution of contribution of wet and dry depositions to total deposition in each type in  
470 WRF-Chem. (b) Distribution of contribution of wet and dry depositions to total deposition for all  
471 depositions, depositions over 90<sup>th</sup>, 95<sup>th</sup>, and 99<sup>th</sup> percentile.  
472  
473

### 474 3.4 Features of the dust transport in MERRA-2

475 We repeated the SOM analyses using 2019 MERRA-2 data to examine the WRF-Chem model  
476 performance and interannual variability. We conducted additional SOM analyses using 2001-2021  
477 climatology MERRA-2 data to investigate the interannual variability of the transport patterns. The low-  
478 level and mid-level dust transport features identified in MERRA-2 (Figs. 11-12) are similar to their  
479 corresponding types in WRF-Chem (Fig. 3), with types 1, 2, 3, and 4 representing MSR, SBJ-related, NPH-  
480 related and CPZ transport, respectively (Fig. 11). Additionally, north-south transport occurs in the middle  
481 layer in type 3 and west-east transport in type 4, despite the slight difference in the peak region (Fig. 12).



482  
 483 **Figure 11** Low-level dust concentration ( $\mu\text{g m}^{-3}$ ) and wind vectors ( $\text{m s}^{-1}$ ) in each of the four SOM types  
 484 from MERRA-2 for the year 2019. The numbers on the top of subplots denote the frequency of each type.



485  
 486 **Figure 12** Mid-level (200-700 hPa average) dust concentration ( $\mu\text{g m}^{-3}$ ) and dust transport fluxes ( $\mu\text{g m}^{-2} \text{s}^{-1}$ ) in each of the four SOM types from MERRA-2 for the year 2019  
 487  
 488

489         The relative contribution of each transport type in MERRA-2 (SBJ-related > MSR > CPZ > NPH-  
 490 related) is generally consistent with the results in WRF-Chem (MSR > SBJ-related > CPZ > NPH-related),  
 491 except that the MSR transport occurs less frequently in MERRA-2. The difference is largely caused by the  
 492 spatial resolution of the two datasets. With a resolution of  $0.5^\circ \times 0.625^\circ$ , MERRA-2 has smooth topography  
 493 information and cannot resolve the high peaks of the Sierra Nevada which produce the MSR winds and  
 494 transport. Consequently, MSR transport contributes to a smaller fraction in the MERRA-2. The coarser  
 495 resolution MERRA-2 also produces a more homogeneous dust concentration at low levels than 2-km WRF-  
 496 Chem.

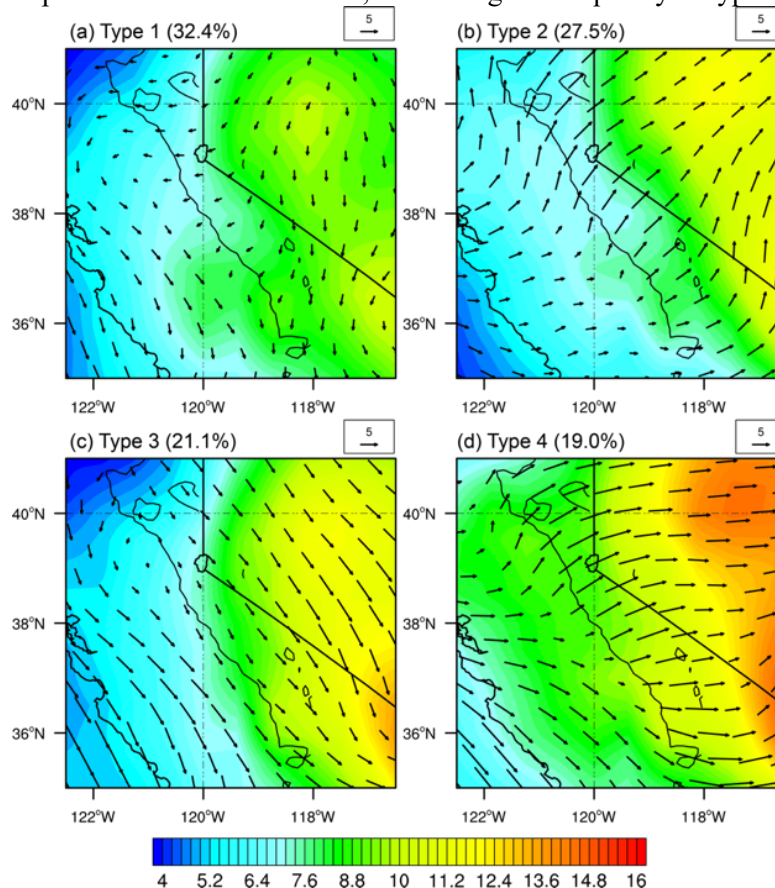
497         Similar dust concentrations and transport patterns are found in the 21-year SOM analysis (Fig. 13),  
 498 indicating that the four patterns identified in 2019 are representative of the climatological conditions. In



499 climatology, the SBJ is weaker and air inflows hit the California coast at a further north latitude (about  
 500 40 °N; Fig. 13b), which is reasonable as 2019 is an El Niño year with stronger AR reaching California  
 501 further south than usual.

502 The changes in the transport patterns reflect the interannual variations of large-scale forcings and  
 503 regional weather conditions, which is investigated using the frequency of each type in a year during 2001-  
 504 2021 (Fig. S4). Types 1 and 4 have a negative correlation coefficient ( $R=-0.75$ ) in their frequency,  
 505 indicating the competing impact between remote transport and local emissions on dust concentrations over  
 506 the Sierra Nevada. Especially, type 4 tends to occur more frequently during La Niña years while less  
 507 frequently during El Niño years. An opposite conclusion can be drawn for type 1.

508 We further examine the dust transport pattern and the frequency of the four SOM types during three La  
 509 Niña (2008, 2011, and 2021) and three El Niño (2015, 2016, and 2019) years. We find that the La Niña  
 510 years have larger dust concentrations than El Niño years in both lower levels and middle levels (Figs. S5-  
 511 S8), due to suppressed precipitations and drier soil in the southwestern U.S. Meanwhile, the frequencies  
 512 of types 3 and 4 are higher in El Niño years, reflecting the increased contribution of cross-Pacific  
 513 transport to dust loading over California. The increase of remote transport weakens the relative  
 514 importance of local emissions, decreasing the frequency of type 1.



515



516 **Figure 13** Low level dust concentration ( $\mu\text{g m}^{-3}$ ) and wind vectors ( $\text{m s}^{-1}$ ) in each of the four SOM types  
517 from MERRA-2 averaged over 2001-2021. The numbers on the top right of subplots denote the frequency  
518 of each type.  
519

520 **4. Conclusions and discussion**



521 **Figure 14** Schematic diagram of typical dust transport patterns across the Sierra Nevada. The “MSR”  
522 demotes mesoscale regional transport. The “SBJ” and “NPH” denotes dust transport dominated by Sierra-  
523 Barrier Jets (SBJ) and North Pacific High (NPH), respectively, while the “CPZ” denotes Cross-Pacific  
524 Zonal transport.  
525  
526

527 With a focus on the dust that influences the mountain snow, we investigated the dust sources  
528 surrounding the Sierra Nevada and their typical transport patterns during the spring and early summer.  
529 Despite the strongest emissions from the Mojave Desert, dust is only transported northward to the mountain  
530 when the mesoscale weather pattern dominates the southwest U.S. (Fig. 14). During 64.25% of our study  
531 period, dust from the Mojave Desert is transported away from the mountains. Dust emitted from the Great  
532 Basin is transported to the central Sierra Nevada during MSR transport and to the eastern part when the

533 NPH builds in the eastern Pacific. It is blown eastward by air inflows from the ocean during SBJ or cross-  
534 Pacific transport. In contrast, dust produced by the Central Valley is persistently transported to the west  
535 mountain slope, playing an essential role in snow impurities there. Carried by intense air inflows, it can be  
536 transported to the lee-side of the Sierra Nevada .

537         During April, Asia dust is transported zonally over the North Pacific through the straight zonal  
538 isobars at the middle level. The dust layer descends to 800 hPa when it reaches the California coast. In the  
539 presence of the NPH, dust emitted from Asia excurses north into Alaska/Canada and travels south along  
540 the U.S. west coast. The dust travels at a higher altitude, and the concentrations are weaker than the zonal  
541 transport.

542         Large amounts of depositions are found on the west slope, which generally decrease with elevations.  
543 Dust particles transported to the higher altitude are small in size and difficult to deposit through gravitational  
544 effects. The SBJ-produced AR collects dust in the rain and snow and deposits it on the high mountain.  
545 Besides, considerable depositions occur when the elevated dust layer from the Pacific collides with the  
546 mountain. We acknowledge that our characterization of dominant transport patterns might be limited by  
547 model uncertainties. Besides, the coarse-resolution reanalyses data, MERRA-2, cannot accurately resolve  
548 the topography effects and tends to underestimate mesoscale regional transport. Furthermore, both WRF-  
549 Chem and MERRA-2 describe dust emissions from dryland by relating them to high wind speed, soil  
550 moisture, and soil type (Ginoux et al., 2001), while dust emission from agricultural lands is not specifically  
551 implemented. However, a comprehensive evaluation of airborne dust and PM<sub>2.5</sub> concentration between  
552 model simulation and site observations in our previous study shows a good agreement between both (Huang  
553 et al., 2022a). In addition, the dust transport pathways have well-defined patterns associated with the  
554 mesoscale and large-scale weather systems. The general consistency across different models (WRF-Chem  
555 and MERRA-2) and observations (satellite analysis) and across different years also give us confidence that  
556 the results are valid despite model uncertainties.

557         The analyses of dust emission and transport can be used to understand dust transport in a changing  
558 climate. Studies have shown that global warming continues to dry the soil, producing more dust emissions

559 over the western U.S. Nevertheless, the change in transport and deposition patterns has not been well  
560 recognized. Our study highlighted the connection between dust transport and dominant weather patterns  
561 across the Sierra Nevada; the latter might respond in a more predictable way to climate change. Future  
562 projections show that global warming may increase the frequency of landfalling AR by 20-35% by the end  
563 of the 21<sup>st</sup> century (Hagos et al., 2016; Rhoades et al., 2021). Besides, the widening of the Hadley Cell in  
564 response to global warming might enhance the NPH and shift it poleward (Song et al., 2018; Choi et al.,  
565 2016). Thus said, the SBJ- and NPH-related dust transport may occur more frequently while the MSR  
566 transport may become less common. In this regard, changes in dust emissions from the Central Valley might  
567 play a more critical role in mountain snow impurities than those from the Mojave Desert and the Great  
568 Basin, producing more depositions on the west slope of the Sierra Nevada.

569

570 **Data availability:**

571 The IASI DOD data is acquired from <https://iasi.aeris-data.fr/dust-aod/>. The MIDAS DOD is acquired from  
572 <https://zenodo.org/record/4244106#.YsJqe-zMIws>. MERRA-2 aerosol reanalyses are available from  
573 <https://disc.gsfc.nasa.gov/datasets?keywords=MERRA2&page=1> and ERA5 wind reanalyses are available  
574 from <https://rda.ucar.edu/datasets/ds633.0/>. The WRF-Chem and MERRA-2 SOM clustering results have  
575 been uploaded to <https://doi.org/10.5281/zenodo.6795994>.

576

577 **Author contributions:**

578 HH performed the analysis and drafted the manuscript. The methodology was developed by HH and YL.  
579 JZ and AG provided the observational data used for model validation. YQ, CH, and ZZ helped with the  
580 analysis and offered valuable comments. All authors contributed to writing and editing the manuscript.

581

582 **Competing interests:**

583 The authors declare that they have no conflict of interest.

584

585 **Acknowledgement:**

586 This research was supported by NASA awards: 80NSSC21K0997, 80NSSC20K1722, 80NSSC20K1349,  
587 and 80NSSC18K1489. Antonis Gkikas was supported by the Hellenic Foundation for Research and  
588 Innovation (H.F.R.I.) under the “2nd Call for H.F.R.I. Research Projects to support Post-Doctoral  
589 Researchers” (project acronym: ATLANTAS, project number: 544). The Pacific Northwest National  
590 Laboratory (PNNL) is operated for DOE by the Battelle Memorial Institute under contract DE-AC05-  
591 76RLO1830.

592 Reference:

- 593 Aarons, S. M., Arvin, L. J., Aciego, S. M., Riebe, C. S., Johnson, K. R., Blakowski, M. A., Koornneef,  
594 J. M., Hart, S. C., Barnes, M. E., Dove, N., Botthoff, J. K., Maltz, M., and Aronson, E. L.: Competing  
595 droughts affect dust delivery to Sierra Nevada, *Aeolian Research*, 41, 100545,  
596 <https://doi.org/10.1016/j.aeolia.2019.100545>, 2019.
- 597 Achakulwisut, P., Shen, L., and Mickley, L. J.: What Controls Springtime Fine Dust Variability in the  
598 Western United States? Investigating the 2002–2015 Increase in Fine Dust in the U.S. Southwest,  
599 *Journal of Geophysical Research: Atmospheres*, 122, 12,449–412,467,  
600 <https://doi.org/10.1002/2017JD027208>, 2017.
- 601 Aciego, S. M., Riebe, C. S., Hart, S. C., Blakowski, M. A., Carey, C. J., Aarons, S. M., Dove, N. C.,  
602 Botthoff, J. K., Sims, K. W. W., and Aronson, E. L.: Dust outpaces bedrock in nutrient supply to  
603 montane forest ecosystems, *Nat Commun*, 8, 14800, 10.1038/ncomms14800, 2017.
- 604 Ault, A. P., Williams, C. R., White, A. B., Neiman, P. J., Creamean, J. M., Gaston, C. J., Ralph, F. M.,  
605 and Prather, K. A.: Detection of Asian dust in California orographic precipitation, *Journal of*  
606 *Geophysical Research: Atmospheres*, 116, <https://doi.org/10.1029/2010JD015351>, 2011.
- 607 Bao, J.-W., Michelson, S. A., Persson, P. O. G., Djalalova, I. V., and Wilczak, J. M.: Observed and  
608 WRF-Simulated Low-Level Winds in a High-Ozone Episode during the Central California Ozone  
609 Study, *Journal of Applied Meteorology and Climatology*, 47, 2372–2394,  
610 10.1175/2008jamc1822.1, 2008.
- 611 Bao, M. and Wallace, J. M.: Cluster Analysis of Northern Hemisphere Wintertime 500-hPa Flow  
612 Regimes during 1920–2014, *J Atmos Sci*, 72, 3597–3608, 10.1175/JAS-D-15-0001.1, 2015.
- 613 Brahney, J., Ballantyne, A. P., Sievers, C., and Neff, J. C.: Increasing Ca<sup>2+</sup> deposition in the western  
614 US: The role of mineral aerosols, *Aeolian Research*, 10, 77–87,  
615 <https://doi.org/10.1016/j.aeolia.2013.04.003>, 2013.
- 616 Buchard, V., da Silva, A. M., Randles, C. A., Colarco, P., Ferrare, R., Hair, J., Hostetler, C., Tackett,  
617 J., and Winker, D.: Evaluation of the surface PM<sub>2.5</sub> in Version 1 of the NASA MERRA Aerosol  
618 Reanalysis over the United States, *Atmos Environ*, 125, 100–111,  
619 <https://doi.org/10.1016/j.atmosenv.2015.11.004>, 2016.
- 620 Buchard, V., Randles, C. A., da Silva, A. M., Darmenov, A., Colarco, P. R., Govindaraju, R., Ferrare,  
621 R., Hair, J., Beyersdorf, A. J., Ziemba, L. D., and Yu, H.: The MERRA-2 Aerosol Reanalysis, 1980  
622 Onward. Part II: Evaluation and Case Studies, *J Climate*, 30, 6851–6872, 10.1175/JCLI-D-16-0613.1,  
623 2017.
- 624 Buchholz, R., Emmons, L., and Tilmes, S.: CESM2. 1/CAM-chem instantaneous output for  
625 boundary conditions, in: UCAR/NCAR-Atmospheric Chemistry Observations and Modeling  
626 Laboratory, 2019.
- 627 Capelle, V., Chédin, A., Pondrom, M., Crevoisier, C., Armante, R., Crepeau, L., and Scott, N. A.:  
628 Infrared dust aerosol optical depth retrieved daily from IASI and comparison with AERONET over  
629 the period 2007–2016, *Remote Sens Environ*, 206, 15–32,  
630 <https://doi.org/10.1016/j.rse.2017.12.008>, 2018.
- 631 Capelle, V., Chédin, A., Siméon, M., Tsamalis, C., Pierangelo, C., Pondrom, M., Crevoisier, C.,  
632 Crepeau, L., and Scott, N. A.: Evaluation of IASI-derived dust aerosol characteristics over the  
633 tropical belt, *Atmos. Chem. Phys.*, 14, 9343–9362, 10.5194/acp-14-9343-2014, 2014.

634 Chapman, E. G., Gustafson, W. I., Easter, R. C., Barnard, J. C., Ghan, S. J., Pekour, M. S., and Fast,  
635 J. D.: Coupling aerosol-cloud-radiative processes in the WRF-Chem model: Investigating the  
636 radiative impact of elevated point sources, *Atmos Chem Phys*, 9, 945-964, 10.5194/acp-9-945-  
637 2009, 2009.

638 Chin, M., Diehl, T., Ginoux, P., and Malm, W.: Intercontinental transport of pollution and dust  
639 aerosols: implications for regional air quality, *Atmos. Chem. Phys.*, 7, 5501-5517, 10.5194/acp-7-  
640 5501-2007, 2007.

641 Chin, M., Ginoux, P., Kinne, S., Torres, O., Holben, B. N., Duncan, B. N., Martin, R. V., Logan, J. A.,  
642 Higurashi, A., and Nakajima, T.: Tropospheric Aerosol Optical Thickness from the GOCART Model  
643 and Comparisons with Satellite and Sun Photometer Measurements, *J Atmos Sci*, 59, 461-483,  
644 10.1175/1520-0469(2002)059<0461:Taotft>2.0.Co;2, 2002.

645 Choi, J., Lu, J., Son, S. W., Frierson, D. M., and Yoon, J. H.: Uncertainty in future projections of the  
646 North Pacific subtropical high and its implication for California winter precipitation change,  
647 *Journal of Geophysical Research: Atmospheres*, 121, 795-806, 2016.

648 Clausnitzer, H. and Singer, M. J.: Environmental influences on respirable dust production from  
649 agricultural operations in California, *Atmos Environ*, 34, 1739-1745,  
650 [https://doi.org/10.1016/S1352-2310\(99\)00385-4](https://doi.org/10.1016/S1352-2310(99)00385-4), 2000.

651 Creamean, J. M., Spackman, J. R., Davis, S. M., and White, A. B.: Climatology of long-range  
652 transported Asian dust along the West Coast of the United States, *Journal of Geophysical*  
653 *Research: Atmospheres*, 119, 12,171-112,185, <https://doi.org/10.1002/2014JD021694>, 2014.

654 Creamean, J. M., Suski, K. J., Rosenfeld, D., Cazorla, A., DeMott, P. J., Sullivan, R. C., White, A. B.,  
655 Ralph, F. M., Minnis, P., and Comstock, J. M.: Dust and biological aerosols from the Sahara and  
656 Asia influence precipitation in the western US, *Science*, 339, 1572-1578, 2013.

657 Crooks, J. L., Cascio, W. E., Percy, M. S., Reyes, J., Neas, L. M., and Hilborn, E. D.: The Association  
658 between Dust Storms and Daily Non-Accidental Mortality in the United States,  
659 1993&#x2013;2005, *Environ Health Persp*, 124, 1735-1743, doi:10.1289/EHP216, 2016.

660 Duniway, M. C., Pfennigwerth, A. A., Fick, S. E., Nauman, T. W., Belnap, J., and Barger, N. N.: Wind  
661 erosion and dust from US drylands: a review of causes, consequences, and solutions in a changing  
662 world, *Ecosphere*, 10, e02650, <https://doi.org/10.1002/ecs2.2650>, 2019.

663 Easter, R. C., Ghan, S. J., Zhang, Y., Saylor, R. D., Chapman, E. G., Laulainen, N. S., Abdul-Razzak,  
664 H., Leung, L. R., Bian, X. D., and Zaveri, R. A.: MIRAGE: Model description and evaluation of  
665 aerosols and trace gases, *J Geophys Res-Atmos*, 109, Artn D20210  
666 10.1029/2004jd004571, 2004.

667 Emmons, L. K., Schwantes, R. H., Orlando, J. J., Tyndall, G., Kinnison, D., Lamarque, J. F., Marsh,  
668 D., Mills, M. J., Tilmes, S., Bardeen, C., Buchholz, R. R., Conley, A., Gettelman, A., Garcia, R.,  
669 Simpson, I., Blake, D. R., Meinardi, S., and Petron, G.: The Chemistry Mechanism in the  
670 Community Earth System Model Version 2 (CESM2), *J Adv Model Earth Sy*, 12, e2019MS001882,  
671 ARTN e2019MS001882  
672 10.1029/2019MS001882, 2020.

673 Forster, P., Ramaswamy, V., Artaxo, P., Berntsen, T., Betts, R., Fahey, D. W., Haywood, J., Lean, J.,  
674 Lowe, D. C., and Myhre, G.: Changes in atmospheric constituents and in radiative forcing. Chapter  
675 2, in: *Climate change 2007. The physical science basis*, 2007.

676 Gelaro, R., McCarty, W., Suarez, M. J., Todling, R., Molod, A., Takacs, L., Randles, C., Darmenov,  
677 A., Bosilovich, M. G., Reichle, R., Wargan, K., Coy, L., Cullather, R., Draper, C., Akella, S., Buchard,

678 V., Conaty, A., da Silva, A., Gu, W., Kim, G. K., Koster, R., Lucchesi, R., Merkova, D., Nielsen, J. E.,  
679 Partyka, G., Pawson, S., Putman, W., Rienecker, M., Schubert, S. D., Sienkiewicz, M., and Zhao, B.:  
680 The Modern-Era Retrospective Analysis for Research and Applications, Version 2 (MERRA-2), J  
681 Clim, Volume 30, 5419-5454, 10.1175/JCLI-D-16-0758.1, 2017.

682 Giannadaki, D., Pozzer, A., and Lelieveld, J.: Modeled global effects of airborne desert dust on air  
683 quality and premature mortality, *Atmos Chem Phys*, 14, 957-968, 2014.

684 Ginoux, P., Prospero, J. M., Gill, T. E., Hsu, N. C., and Zhao, M.: Global-scale attribution of  
685 anthropogenic and natural dust sources and their emission rates based on MODIS Deep Blue  
686 aerosol products, *Reviews of Geophysics*, 50, <https://doi.org/10.1029/2012RG000388>, 2012.

687 Ginoux, P., Chin, M., Tegen, I., Prospero, J. M., Holben, B., Dubovik, O., and Lin, S. J.: Sources and  
688 distributions of dust aerosols simulated with the GOCART model, *J Geophys Res-Atmos*, 106,  
689 20255-20273, Doi 10.1029/2000jd000053, 2001.

690 Gkikas, A., Proestakis, E., Amiridis, V., Kazadzis, S., Di Tomaso, E., Marinou, E., Hatzianastassiou,  
691 N., Kok, J. F., and García-Pando, C. P.: Quantification of the dust optical depth across  
692 spatiotemporal scales with the MIDAS global dataset (2003–2017), *Atmos. Chem. Phys.*, 22, 3553-  
693 3578, 10.5194/acp-22-3553-2022, 2022.

694 Gkikas, A., Proestakis, E., Amiridis, V., Kazadzis, S., Di Tomaso, E., Tsekeri, A., Marinou, E.,  
695 Hatzianastassiou, N., and Pérez García-Pando, C.: ModIs Dust AeroSol (MIDAS): a global fine-  
696 resolution dust optical depth data set, *Atmos. Meas. Tech.*, 14, 309-334, 10.5194/amt-14-309-  
697 2021, 2021.

698 Goldstein, H. L., Breit, G. N., and Reynolds, R. L.: Controls on the chemical composition of saline  
699 surface crusts and emitted dust from a wet playa in the Mojave Desert (USA), *J Arid Environ*, 140,  
700 50-66, <https://doi.org/10.1016/j.jaridenv.2017.01.010>, 2017.

701 Hagos, S. M., Leung, L. R., Yoon, J.-H., Lu, J., and Gao, Y.: A projection of changes in landfalling  
702 atmospheric river frequency and extreme precipitation over western North America from the  
703 Large Ensemble CESM simulations, *Geophys Res Lett*, 43, 1357-1363,  
704 <https://doi.org/10.1002/2015GL067392>, 2016.

705 Hand, J. L., Gill, T. E., and Schichtel, B. A.: Spatial and seasonal variability in fine mineral dust and  
706 coarse aerosol mass at remote sites across the United States, *Journal of Geophysical Research:*  
707 *Atmospheres*, 122, 3080-3097, <https://doi.org/10.1002/2016JD026290>, 2017.

708 Hand, J. L., White, W. H., Gebhart, K. A., Hyslop, N. P., Gill, T. E., and Schichtel, B. A.: Earlier onset  
709 of the spring fine dust season in the southwestern United States, *Geophys Res Lett*, 43, 4001-  
710 4009, <https://doi.org/10.1002/2016GL068519>, 2016.

711 Hannachi, A.: On the origin of planetary-scale extratropical winter circulation regimes, *J Atmos*  
712 *Sci*, 67, 1382-1401, 2010.

713 Haywood, J. M., Allan, R. P., Culverwell, I., Slingo, T., Milton, S., Edwards, J., and Clerbaux, N.: Can  
714 desert dust explain the outgoing longwave radiation anomaly over the Sahara during July 2003?,  
715 *Journal of Geophysical Research: Atmospheres*, 110, <https://doi.org/10.1029/2004JD005232>,  
716 2005.

717 Hersbach, H., Bell, B., Berrisford, P., Hirahara, S., Horanyi, A., Muñoz-Sabater, J., Nicolas, J.,  
718 Peubey, C., Radu, R., Schepers, D., Simmons, A., Soci, C., Abdalla, S., Abellan, X., Balsamo, G.,  
719 Bechtold, P., Biavati, G., Bidlot, J., Bonavita, M., De Chiara, G., Dahlgren, P., Dee, D., Diamantakis,  
720 M., Dragani, R., Flemming, J., Forbes, R., Fuentes, M., Geer, A., Haimberger, L., Healy, S., Hogan,  
721 R. J., Holm, E., Janiskova, M., Keeley, S., Laloyaux, P., Lopez, P., Lupu, C., Radnoti, G., de Rosnay,



722 P., Rozum, I., Vamborg, F., Villaume, S., and Thepaut, J. N.: The ERA5 global reanalysis, *Q J Roy*  
723 *Meteor Soc*, 146, 1999-2049, 10.1002/qj.3803, 2020.

724 Hilton, F., Armante, R., August, T., Barnet, C., Bouchard, A., Camy-Peyret, C., Capelle, V., Clarisse,  
725 L., Clerbaux, C., Coheur, P. F., Collard, A., Crevoisier, C., Dufour, G., Edwards, D., Faijan, F., Fourrie,  
726 N., Gambacorta, A., Goldberg, M., Guidard, V., Hurtmans, D., Illingworth, S., Jacquinet-Husson,  
727 N., Kerzenmacher, T., Klaes, D., Lavanant, L., Masiello, G., Matricardi, M., McNally, A., Newman,  
728 S., Pavelin, E., Payan, S., Pequignot, E., Peyridieu, S., Phulpin, T., Remedios, J., Schlusser, P., Serio,  
729 C., Strow, L., Stubenrauch, C., Taylor, J., Tobin, D., Wolf, W., and Zhou, D.: HYPERSPECTRAL EARTH  
730 OBSERVATION FROM IASI Five Years of Accomplishments, *B Am Meteorol Soc*, 93, 347-370,  
731 10.1175/Bams-D-11-00027.1, 2012.

732 Huang, H., Gu, Y., Xue, Y., Jiang, J., and Zhao, B.: Assessing aerosol indirect effect on clouds and  
733 regional climate of East/South Asia and West Africa using NCEP GFS, *Clim Dyn*, 52, 5759-5774,  
734 10.1007/s00382-018-4476-9, 2019.

735 Huang, H., Qian, Y., He, C., Bair, E. H., and Rittger, K.: Snow Albedo Feedbacks Enhance Snow  
736 Impurity-Induced Radiative Forcing in the Sierra Nevada, *Geophys Res Lett*, 49, e2022GL098102,  
737 <https://doi.org/10.1029/2022GL098102>, 2022a.

738 Huang, H., Fischella, M. R., Liu, Y., Ban, Z., Fayne, J. V., Li, D., Cavanaugh, K. C., and Lettenmaier,  
739 D. P.: Changes in Mechanisms and Characteristics of Western U.S. Floods Over the Last Sixty Years,  
740 *Geophys Res Lett*, 49, e2021GL097022, 10.1029/2021gl097022, 2022b.

741 Hunt, W. H., Winker, D. M., Vaughan, M. A., Powell, K. A., Lucker, P. L., and Weimer, C.: CALIPSO  
742 Lidar Description and Performance Assessment, *Journal of Atmospheric and Oceanic Technology*,  
743 26, 1214-1228, 10.1175/2009jtech1223.1, 2009.

744 Jardine, G. E., Crocker, A. J., Bailey, I., Cooper, M. J., Milton, J. A., and Wilson, P. A.: The imprint  
745 of windblown dust from the North American Southwest on the California Channel Islands and  
746 Pacific Ocean sediments, *Quaternary Science Reviews*, 261, 106934,  
747 <https://doi.org/10.1016/j.quascirev.2021.106934>, 2021.

748 Kim, D., Chin, M., Cruz, C. A., Tong, D., and Yu, H.: Spring Dust in Western North America and Its  
749 Interannual Variability—Understanding the Role of Local and Transported Dust, *Journal of*  
750 *Geophysical Research: Atmospheres*, 126, e2021JD035383,  
751 <https://doi.org/10.1029/2021JD035383>, 2021.

752 Kim, M. H., Omar, A. H., Tackett, J. L., Vaughan, M. A., Winker, D. M., Trepte, C. R., Hu, Y., Liu, Z.,  
753 Poole, L. R., Pitts, M. C., Kar, J., and Magill, B. E.: The CALIPSO version 4 automated aerosol  
754 classification and lidar ratio selection algorithm, *Atmos. Meas. Tech.*, 11, 6107-6135,  
755 10.5194/amt-11-6107-2018, 2018.

756 Laden, F., Schwartz, J., Speizer, F. E., and Dockery, D. W.: Reduction in fine particulate air pollution  
757 and mortality: Extended follow-up of the Harvard Six Cities study, *Am J Respir Crit Care Med*, 173,  
758 667-672, 10.1164/rccm.200503-443OC, 2006.

759 Lei, H. and Wang, J. X. L.: Observed characteristics of dust storm events over the western United  
760 States using meteorological, satellite, and air quality measurements, *Atmos. Chem. Phys.*, 14,  
761 7847-7857, 10.5194/acp-14-7847-2014, 2014.

762 Lim, S. S., Vos, T., Flaxman, A. D., Danaei, G., Shibuya, K., Adair-Rohani, H., AlMazroa, M. A.,  
763 Amann, M., Anderson, H. R., Andrews, K. G., Aryee, M., Atkinson, C., Bacchus, L. J., Bahalim, A.  
764 N., Balakrishnan, K., Balmes, J., Barker-Collo, S., Baxter, A., Bell, M. L., Blore, J. D., Blyth, F., Bonner,  
765 C., Borges, G., Bourne, R., Boussinesq, M., Brauer, M., Brooks, P., Bruce, N. G., Brunekreef, B.,



766 Bryan-Hancock, C., Bucello, C., Buchbinder, R., Bull, F., Burnett, R. T., Byers, T. E., Calabria, B.,  
767 Carapetis, J., Carnahan, E., Chafe, Z., Charlson, F., Chen, H., Chen, J. S., Cheng, A. T.-A., Child, J. C.,  
768 Cohen, A., Colson, K. E., Cowie, B. C., Darby, S., Darling, S., Davis, A., Degenhardt, L., Dentener, F.,  
769 Des Jarlais, D. C., Devries, K., Dherani, M., Ding, E. L., Dorsey, E. R., Driscoll, T., Edmond, K., Ali, S.  
770 E., Engell, R. E., Erwin, P. J., Fahimi, S., Falder, G., Farzadfar, F., Ferrari, A., Finucane, M. M.,  
771 Flaxman, S., Fowkes, F. G. R., Freedman, G., Freeman, M. K., Gakidou, E., Ghosh, S., Giovannucci,  
772 E., Gmel, G., Graham, K., Grainger, R., Grant, B., Gunnell, D., Gutierrez, H. R., Hall, W., Hoek, H.  
773 W., Hogan, A., Hosgood, H. D., Hoy, D., Hu, H., Hubbell, B. J., Hutchings, S. J., Ibeanusi, S. E.,  
774 Jacklyn, G. L., Jasrasaria, R., Jonas, J. B., Kan, H., Kanis, J. A., Kassebaum, N., Kawakami, N., Khang,  
775 Y.-H., Khatibzadeh, S., Khoo, J.-P., Kok, C., Laden, F., Lalloo, R., Lan, Q., Lathlean, T., Leasher, J. L.,  
776 Leigh, J., Li, Y., Lin, J. K., Lipshultz, S. E., London, S., Lozano, R., Lu, Y., Mak, J., Malekzadeh, R.,  
777 Mallinger, L., Marcenes, W., March, L., Marks, R., Martin, R., McGale, P., McGrath, J., Mehta, S.,  
778 Memish, Z. A., Mensah, G. A., Merriman, T. R., Micha, R., Michaud, C., Mishra, V., Hanafiah, K. M.,  
779 Mokdad, A. A., Morawska, L., Mozaffarian, D., Murphy, T., Naghavi, M., Neal, B., Nelson, P. K.,  
780 Nolla, J. M., Norman, R., Olives, C., Omer, S. B., Orchard, J., Osborne, R., Ostro, B., Page, A.,  
781 Pandey, K. D., Parry, C. D. H., Passmore, E., Patra, J., Pearce, N., Pelizzari, P. M., Petzold, M.,  
782 Phillips, M. R., Pope, D., Pope, C. A., Powles, J., Rao, M., Razavi, H., Rehfuss, E. A., Rehm, J. T.,  
783 Ritz, B., Rivara, F. P., Roberts, T., Robinson, C., Rodriguez-Portales, J. A., Romieu, I., Room, R.,  
784 Rosenfeld, L. C., Roy, A., Rushton, L., Salomon, J. A., Sampson, U., Sanchez-Riera, L., Sanman, E.,  
785 Sapkota, A., Seedat, S., Shi, P., Shield, K., Shivakoti, R., Singh, G. M., Sleet, D. A., Smith, E., Smith,  
786 K. R., Stapelberg, N. J. C., Steenland, K., Stöckl, H., Stovner, L. J., Straif, K., Straney, L., Thurston,  
787 G. D., Tran, J. H., Van Dingenen, R., van Donkelaar, A., Veerman, J. L., Vijayakumar, L., Weintraub,  
788 R., Weissman, M. M., White, R. A., Whiteford, H., Wiersma, S. T., Wilkinson, J. D., Williams, H. C.,  
789 Williams, W., Wilson, N., Woolf, A. D., Yip, P., Zielinski, J. M., Lopez, A. D., Murray, C. J. L., and  
790 Ezzati, M.: A comparative risk assessment of burden of disease and injury attributable to 67 risk  
791 factors and risk factor clusters in 21 regions, 1990–2010: a systematic analysis for the Global  
792 Burden of Disease Study 2010, *The Lancet*, 380, 2224-2260, [https://doi.org/10.1016/S0140-](https://doi.org/10.1016/S0140-6736(12)61766-8)  
793 [6736\(12\)61766-8](https://doi.org/10.1016/S0140-6736(12)61766-8), 2012.

794 Liu, Y., Qian, Y., and Berg, L. K.: Local-thermal-gradient and large-scale-circulation impacts on  
795 turbine-height wind speed forecasting over the Columbia River Basin, *Wind Energ. Sci.*, 7, 37-51,  
796 10.5194/wes-7-37-2022, 2022.

797 Muhs, D. R., Budahn, J., Reheis, M., Beann, J., Skipp, G., and Fisher, E.: Airborne dust transport to  
798 the eastern Pacific Ocean off southern California: Evidence from San Clemente Island, *Journal of*  
799 *Geophysical Research: Atmospheres*, 112, <https://doi.org/10.1029/2006JD007577>, 2007.

800 Neff, J. C., Ballantyne, A. P., Farmer, G. L., Mahowald, N. M., Conroy, J. L., Landry, C. C., Overpeck,  
801 J. T., Painter, T. H., Lawrence, C. R., and Reynolds, R. L.: Increasing eolian dust deposition in the  
802 western United States linked to human activity, *Nat Geosci*, 1, 189-195, 10.1038/ngeo133, 2008.

803 Neiman, P. J., Hughes, M., Moore, B. J., Ralph, F. M., and Sukovich, E. M.: Sierra Barrier Jets,  
804 Atmospheric Rivers, and Precipitation Characteristics in Northern California: A Composite  
805 Perspective Based on a Network of Wind Profilers, *Mon Weather Rev*, 141, 4211-4233,  
806 10.1175/mwr-d-13-00112.1, 2013.

807 Okin, G., Gillette, D., and Herrick, J.: Multi-scale controls on and consequences of aeolian  
808 processes in landscape change in arid and semi-arid environments, *J Arid Environ*, 65, 253-275,  
809 2006.

810 Pappagianis, D. and Einstein, H.: Tempest from Tehachapi takes toll or Coccidioides conveyed  
811 aloft and afar, *Western Journal of Medicine*, 129, 527, 1978.

812 Pu, B. and Ginoux, P.: How reliable are CMIP5 models in simulating dust optical depth?, *Atmos.*  
813 *Chem. Phys.*, 18, 12491-12510, 10.5194/acp-18-12491-2018, 2018.

814 Qian, Y., Gustafson, W. I., Leung, L. R., and Ghan, S. J.: Effects of soot-induced snow albedo change  
815 on snowpack and hydrological cycle in western United States based on Weather Research and  
816 Forecasting chemistry and regional climate simulations, *J Geophys Res-Atmos*, 114, Artn D03108  
817 10.1029/2008jd011039, 2009.

818 Qian, Y., Yasunari, T. J., Doherty, S. J., Flanner, M. G., Lau, W. K. M., Ming, J., Wang, H., Wang, M.,  
819 Warren, S. G., and Zhang, R.: Light-absorbing particles in snow and ice: Measurement and  
820 modeling of climatic and hydrological impact, *Adv Atmos Sci*, 32, 64-91, 10.1007/s00376-014-  
821 0010-0, 2014.

822 Randles, C. A., Da Silva, A. M., Buchard, V., Colarco, P. R., Darmenov, A., Govindaraju, R., Smirnov,  
823 A., Holben, B., Ferrare, R., Hair, J., Shinozuka, Y., and Flynn, C. J.: The MERRA-2 Aerosol Reanalysis,  
824 1980 - onward, Part I: System Description and Data Assimilation Evaluation, *J Clim*, 30, 6823-6850,  
825 10.1175/JCLI-D-16-0609.1, 2017.

826 Reheis, M. C. and Kihl, R.: Dust Deposition in Southern Nevada and California, 1984-1989 -  
827 Relations to Climate, Source Area, and Source Lithology, *J Geophys Res-Atmos*, 100, 8893-8918,  
828 Doi 10.1029/94jd03245, 1995.

829 Reusch, D. B., Alley, R. B., and Hewitson, B. C.: North Atlantic climate variability from a self-  
830 organizing map perspective, *Journal of Geophysical Research: Atmospheres*, 112,  
831 <https://doi.org/10.1029/2006JD007460>, 2007.

832 Rhoades, A. M., Risser, M. D., Stone, D. A., Wehner, M. F., and Jones, A. D.: Implications of  
833 warming on western United States landfalling atmospheric rivers and their flood damages,  
834 *Weather Clim Extreme*, 32, 100326, <https://doi.org/10.1016/j.wace.2021.100326>, 2021.

835 Rodionov, S. N., Bond, N. A., and Overland, J. E.: The Aleutian Low, storm tracks, and winter  
836 climate variability in the Bering Sea, *Deep Sea Research Part II: Topical Studies in Oceanography*,  
837 54, 2560-2577, <https://doi.org/10.1016/j.dsr2.2007.08.002>, 2007.

838 Sarangi, C., Qian, Y., Rittger, K., Leung, L. R., Chand, D., Bormann, K. J., and Painter, T. H.: Dust  
839 dominates high-altitude snow darkening and melt over high-mountain Asia, *Nat Clim Change*, 10,  
840 1045+, 10.1038/s41558-020-00909-3, 2020.

841 Skiles, S. M., Flanner, M., Cook, J. M., Dumont, M., and Painter, T. H.: Radiative forcing by light-  
842 absorbing particles in snow, *Nat Clim Change*, 8, 964-971, 10.1038/s41558-018-0296-5, 2018.

843 Song, F., Leung, L. R., Lu, J., and Dong, L.: Future Changes in Seasonality of the North Pacific and  
844 North Atlantic Subtropical Highs, *Geophys Res Lett*, 45, 11,959-911,968,  
845 <https://doi.org/10.1029/2018GL079940>, 2018.

846 Song, F., Feng, Z., Leung, L. R., Houze Jr, R. A., Wang, J., Hardin, J., and Homeyer, C. R.: Contrasting  
847 Spring and Summer Large-Scale Environments Associated with Mesoscale Convective Systems  
848 over the U.S. Great Plains, *J Climate*, 32, 6749-6767, 10.1175/JCLI-D-18-0839.1, 2019.

849 Song, Q., Zhang, Z., Yu, H., Ginoux, P., and Shen, J.: Global dust optical depth climatology derived  
850 from CALIOP and MODIS aerosol retrievals on decadal timescales: regional and interannual  
851 variability, *Atmos. Chem. Phys.*, 21, 13369-13395, 10.5194/acp-21-13369-2021, 2021.

852 Tong, D. Q., Wang, J. X. L., Gill, T. E., Lei, H., and Wang, B.: Intensified dust storm activity and  
853 Valley fever infection in the southwestern United States, *Geophys Res Lett*, 44, 4304-4312,  
854 <https://doi.org/10.1002/2017GL073524>, 2017.

855 Vicars, W. C. and Sickman, J. O.: Mineral dust transport to the Sierra Nevada, California: Loading  
856 rates and potential source areas, *J Geophys Res-Bioge*, 116, Artn G01018  
857 10.1029/2010jg001394, 2011.

858 Vigaud, N. and Robertson, A. W.: Convection regimes and tropical-midlatitude interactions over  
859 the Intra-American Seas from May to November, *Int J Climatol*, 37, 987-1000, 2017.

860 Vigaud, N., Robertson, A. W., and Tippett, M. K.: Predictability of recurrent weather regimes over  
861 North America during winter from submonthly reforecasts, *Mon Weather Rev*, 146, 2559-2577,  
862 2018.

863 Visbeck, M. H., Hurrell, J. W., Polvani, L., and Cullen, H. M.: The North Atlantic Oscillation: past,  
864 present, and future, *Proceedings of the National Academy of Sciences*, 98, 12876-12877, 2001.

865 von Storch, H., Langenberg, H., and Feser, F.: A spectral nudging technique for dynamical  
866 downscaling purposes, *Mon Weather Rev*, 128, 3664-3673, 2000.

867 Voss, K. K. and Evan, A. T.: A New Satellite-Based Global Climatology of Dust Aerosol Optical  
868 Depth, *Journal of Applied Meteorology and Climatology*, 59, 83-102, 10.1175/JAMC-D-19-0194.1,  
869 2020.

870 Voss, K. K., Evan, A. T., and Ralph, F. M.: Evaluating the Meteorological Conditions Associated  
871 With Dusty Atmospheric Rivers, *Journal of Geophysical Research: Atmospheres*, 126,  
872 e2021JD035403, <https://doi.org/10.1029/2021JD035403>, 2021.

873 Winker, D. M., Vaughan, M. A., Omar, A., Hu, Y. X., Powell, K. A., Liu, Z. Y., Hunt, W. H., and Young,  
874 S. A.: Overview of the CALIPSO Mission and CALIOP Data Processing Algorithms, *Journal of*  
875 *Atmospheric and Oceanic Technology*, 26, 2310-2323, 10.1175/2009jtecha1281.1, 2009.

876 Winker, D. M., Pelon, J., Coakley, J. A., Ackerman, S. A., Charlson, R. J., Colarco, P. R., Flamant, P.,  
877 Fu, Q., Hoff, R. M., Kittaka, C., Kubar, T. L., Le Treut, H., McCormick, M. P., Megie, G., Poole, L.,  
878 Powell, K., Trepte, C., Vaughan, M. A., and Wielicki, B. A.: THE CALIPSO MISSION A Global 3D View  
879 of Aerosols and Clouds, *B Am Meteorol Soc*, 91, 1211-1229, 10.1175/2010bams3009.1, 2010.

880 Wu, L. T., Su, H., Kalashnikova, O. V., Jiang, J. H., Zhao, C., Garay, M. J., Campbell, J. R., and Yu, N.  
881 P.: WRF-Chem simulation of aerosol seasonal variability in the San Joaquin Valley, *Atmos Chem*  
882 *Phys*, 17, 7291-7309, 10.5194/acp-17-7291-2017, 2017.

883 Wu, L. T., Gu, Y., Jiang, J. H., Su, H., Yu, N. P., Zhao, C., Qian, Y., Zhao, B., Liou, K. N., and Choi, Y.  
884 S.: Impacts of aerosols on seasonal precipitation and snowpack in California based on convection-  
885 permitting WRF-Chem simulations, *Atmos Chem Phys*, 18, 5529-5547, 10.5194/acp-18-5529-  
886 2018, 2018.

887 Young, S. A., Vaughan, M. A., Garnier, A., Tackett, J. L., Lambeth, J. D., and Powell, K. A.: Extinction  
888 and optical depth retrievals for CALIPSO's Version 4 data release, *Atmospheric Measurement*  
889 *Techniques*, 11, 5701-5727, 10.5194/amt-11-5701-2018, 2018.

890 Yu, H., Tan, Q., Chin, M., Remer, L. A., Kahn, R. A., Bian, H., Kim, D., Zhang, Z., Yuan, T., Omar, A.  
891 H., Winker, D. M., Levy, R. C., Kalashnikova, O., Crepeau, L., Capelle, V., and Chédin, A.: Estimates  
892 of African Dust Deposition Along the Trans-Atlantic Transit Using the Decadelong Record of  
893 Aerosol Measurements from CALIOP, MODIS, MISR, and IASI, *Journal of Geophysical Research:*  
894 *Atmospheres*, 124, 7975-7996, <https://doi.org/10.1029/2019JD030574>, 2019.

895 Zaveri, R. A. and Peters, L. K.: A new lumped structure photochemical mechanism for large-scale  
896 applications, *Journal of Geophysical Research: Atmospheres*, 104, 30387-30415, 1999.  
897 Zheng, J., Zhang, Z., Garnier, A., Yu, H., Song, Q., Wang, C., Dubuisson, P., and Di Biagio, C.: The  
898 thermal infrared optical depth of mineral dust retrieved from integrated CALIOP and IIR  
899 observations, *Remote Sens Environ*, 270, 112841, <https://doi.org/10.1016/j.rse.2021.112841>,  
900 2022.  
901